The effect of Niobium on the defect chemistry and corrosion kinetics of tetragonal ZrO2: A density functional theory study

Uuganbayar Otgonbaatar

Submitted to the department of Nuclear Science and Engineering

In partial fulfillment of the requirements for the degrees of

Master of Science in Nuclear Engineering

and

Bachelor of Science in Nuclear Engineering

at the

MASSACHUSETTS INSTITUTE OF TECHNOLOGY

JUNE 2013

©2013 Massachusetts Institute of Technology

All rights reserved

ARCHIVES
MASSACHUSETTS INSTITUTE OF TECHNOLOGY
JUL 16 2013
LIBRARIES

Signature of Author: _____
Uuganbayar Otgonbaatar

Certified by: _____
Bilge Yildiz, Ph.D
Associate Professor of Nuclear Science and Engineering
Thesis supervisor

Certified by: _____
Ju Li, Ph.D
Battelle Energy Alliance Professor of Nuclear Science and Engineering
Professor of Materials Science and Engineering
Thesis reader

Accepted by: _____
Mujid S. Kazimi, Ph.D
TEPCO Professor of Nuclear Science and Engineering
Chair, Department Committee on Graduate Students

The effect of Niobium and strain on the defect chemistry and corrosion kinetics of tetragonal ZrO2: A density functional theory study

Uuganbayar Otgonbaatar

Submitted to the Department of Nuclear Science and Engineering in partial fulfillment of the requirements for the degrees of Master of Science in Nuclear Science and Engineering, Bachelor of Science in Nuclear Science and Engineering on May 10, 2013.

Abstract

Advanced Zirconium based alloys used in the nuclear industry today, such as **ZIRLO^{TM}** , M5 contain up to wt 1.2% Niobium [8]. Experimental effort to determine the effect of Nb on corrosion behaviour of these alloys has no clear answer to whether Nb improves or degrades the corrosion resistance[8, 48, 20]. Even the charge state of Nb as a defect in zirconia is debated. Experimental findings of Froideval et al [5] indicate charge state between +2 and +4 whereas other authors assume it to be +5 [21, 31, 34]. In order to uncover the role of Nb on the local oxide protectiveness we employed ab initio Density Functional Theory (DFT) calculations, and assessed the effect of Niobium on the point defect equilibria in tetragonal zirconia which is critical in the oxide protectiveness [8] among other phases of zirconia. DFT calculated defect formation energies are adjusted for finite temperature effects by accounting for thermal vibrations. Adjusted defect formation energies are then used to construct Kröger-Vink diagram for defect equilibrium concentrations at applicable pO2 levels. The Kröger-Vink diagrams for Nb containing zirconia was compared to that of pure t-Zirconia in order to isolate the changes due to Nb.

Nb is treated as point defect in the oxide. Among the considered point defects and defect complexes of $\mathbf{Nb_{Zr}}$,$\mathbf{Nb_i}$, $\mathbf{Nb_{Zr} - V_O}$ and $\mathbf{Nb_{Zr} - O_i}$, the substitutional point defect $\mathbf{Nb_{Zr}}$ was found to have the lowest free energy of formation, and the highest equilibrium concentration. Nb substitutional point defect, $\mathbf{Nb_{Zr}}$, is found to be stable for Nb+3, Nb+4, Nb+5 charge states while Nb+5 has the highest concentration. The effect of applied external compressive strain on the energetics and stress of different types of defects, and formation energy is quantified as a function of strain. It is observed that the more positively charged the defect, the formation energy increases less as compressive strain is applied. Compared to pure T-ZrO2, ~100 times increase in Zirconium vacancy concentration accompanied by a ~5 times decrease in the doubly charged oxygen vacancy concentration was found due to the presence of Niobium in the high oxygen partial pressure (pO2) regime corresponding to oxide/water interface. This change implies slowing down of oxygen diffusion from surface to bulk, while accelerating oxygen exchange on the surface. Diffusion of zirconium ion to the surface will also accelerate as available point defect concentration increases due to Nb. The increased concentration of $\mathbf{Nb_{Zr}}$ defect with increasing oxygen partial pressure is consistent with our experimental findings in a parallel work in our group[47].

Thesis Supervisor: Bilge Yildiz, Ph.D

Title:Associate Professor of Nuclear Science and Engineering

Thesis Reader: Ju Li, Ph.D

Title:Battelle Energy Alliance Professor of Nuclear Science and Engineering Professor of Materials Science and Engineering

Acknowledgement

I would like to first thank Professor Bilge Yildiz, for great support and mentorship. I am grateful for the UROP opportunity that she provided to me which started me on this project and really opened my eyes into research in computational materials science. She welcomed me to her research group with full heart, and I have gained invaluable experience from interactions with group members and weekly meetings. Moreover, the funding and the generous access she granted me to the computational resource both here at MIT and at Texas Advanced Computational Center made possible this thesis. I am grateful to her for helping me make a transition from being an undergraduate who is not familiar with academic world to being a graduate student. All work in this thesis would not have been possible without her unwavering support for me.

Secondly, I am infinitely grateful to Mostafa Youssef for his mentorship and great help in realizing this thesis. I would not have been able to accomplish any of this work without his mentorship and countless number of meetings and emails that taught me how to do computations, resolve problems, to model phenomenon using solid state physics and so on. I thank you for being there whenever I encountered problems or did not know how to interpret results, and for you taking the time to explain everything and making sure I understood. Majority of the work of my thesis is based on your previous work on native defects in zirconia, and current work on hydrogen defects. Therefore, I consider my work to be an extension to your work and it would not have been possible without the basic framework you developed.

I am also grateful to the members of Laboratory for Electrochemical Interfaces at MIT for their valuable discussions and support.

My master's study would not be possible without the financial support from National Academy for Nuclear Training, and LDRD program at Idaho National Laboratory. For these supports, I am grateful.

Contents

List of Tables

List of Figures

1 Introduction to the corrosion problem of Nb containing Zirconium based alloys

1.1 Application of Zr based alloys

Zirconium based alloys are used in the nuclear industry as fuel cladding and pressure tubes owing to their neutronics and thermal properties. There are other applications of these alloys such as biomedical[31]. Oxidation of Zirconium based alloys is an important research topic and advanced alloys have been engineered for better corrosion resistance. Traditional Zr based alloys contain alloying Fe, Cr and Ni whereas modern advanced alloys have varying content of Niobium Zr-2.5Nb (wt 2.5% Nb), ZIRLO^{TM} (wt 1% Nb) as presented in Table 1 [8]. The aim of the current work is to computationally isolate the effect of Niobium on corrosion of the Zr based alloys.

Alloy	**Nb content (%wt)**
ZIRLO	1.0
M5	0.8-1.2
Zr2.5Nb	2.4-2.8
E110	1.0
Zircaloy4	-
Zircaloy2	-

Table 1: Niobium content of current commercial Zr based alloys

1.2 Microstructure of metal and oxide

At room temperature, as can be projected from Figure 2, Zr-Nb alloys exist in equilibrium structure of separate hexagonal α-Zr, and cubic Nb. It is due to the low solubility of Nb in Zirconium below its eutectoid temperature of 620°**C**. Upon exposure to oxidizing environment, Zr is expected to preferentially oxidize first because the equilibrium pO2 for Zr/ZrO2 interface is about log$\mathbf{pO_2}$=-56 is significantly lower than that of Nb/NbO which is log$\mathbf{pO_2}$=-32. At higher oxygen partial pressure, $\mathbf{Nb_2O_5}$ oxide phase is stable and the phase

equilibrium diagram between $\mathbf{Nb_2O_5}$ and $\mathbf{ZrO_2}$ is given in Figure 2. Based on this diagram, at the Nb alloy concentration of interest Zr-2.5Nb or lower, we expect the Niobium oxide to dissolve in ZrO2 forming a solid solution[31]. Hobbs et al suggest a oxidation reaction mechanism, in Nb-Zr alloys as given in Figure 3.

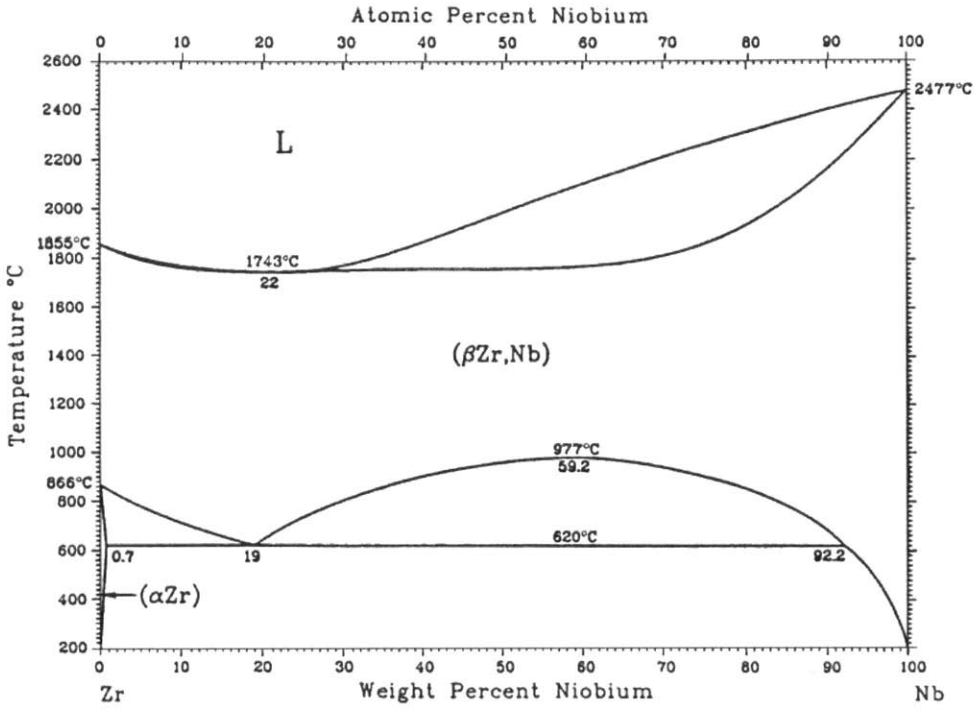

Figure 1: Phase diagram of Niobium and Zirconium mixture

Zirconium oxide which forms upon corrosion of Zr metal is stable in monoclinic phase in room temperature and tetragonal phase is stabilized above around 1440K[31, 37]. A number of experimental works have shown that tetragonal phase exists in higher fraction closer to the metal oxide interface due to compressive stress arising from lattice mismatch at the interface and decreases further away as shown in Figure 4[8, 32]. In nuclear reactors, clad temperature stays well below 1440K during normal operation, and the presence of tetragonal phase is attributed to compressive stress induced by lattice mismatch at the metal/oxide interface [22]. Furthermore, there is evidence that higher tetragonal ZrO2 fraction is correlated with higher corrosion rate [8], therefore this work studies the tetragonal phase of zirconia.

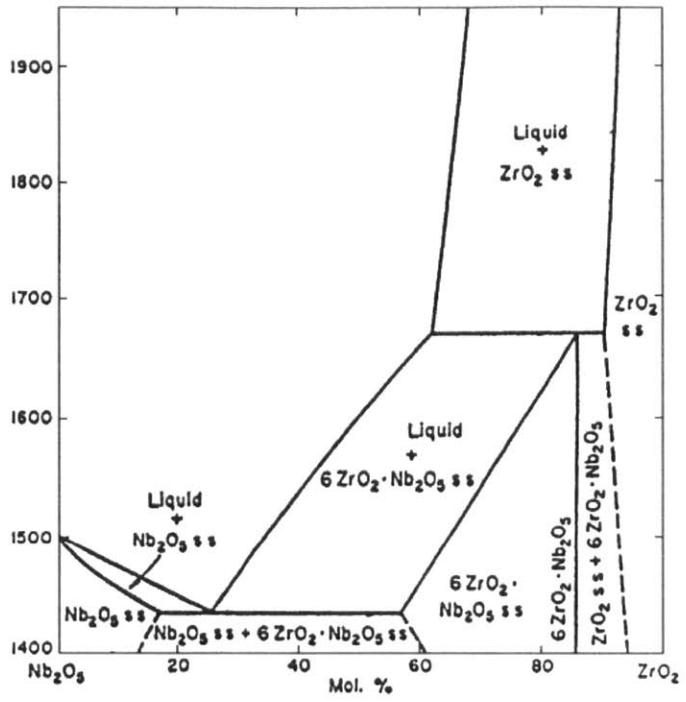

Figure 2: Phase diagram of Niobia and Zirconia mixture[31]

$$\underset{}{O_2 + \alpha\text{-Zr}} \rightarrow \underset{\leq 28.5\ \text{wt\%O}}{\alpha\text{-Zr(O)}} \rightarrow \underset{> 10^{-56}\ \text{atm}\ O_2}{m\text{-}ZrO_2}$$

$$O_2 + \beta\text{-Zr} \rightarrow \underset{\leq 28.5\ \text{wt\%O}}{\alpha\text{-Zr(O)}} + \underset{> 19\ \text{wt\%Nb}}{\beta\text{-Zr(enr)}} \text{ or } \underset{\leq 7\ \text{wt\%Zr}}{\beta\text{-Nb}}$$

$$\rightarrow \underset{> 10^{-56}\ \text{atm}\ O_2}{m\text{-}ZrO_2} + \underset{> 10^{-30}\ \text{atm}\ O_2}{NbO_x} \rightarrow \underset{> 10^{-26}\ \text{atm}\ O_2}{m\text{-}ZrO_2 + 6ZrO_2 \cdot Nb_2O_5}$$

$$O_2 + \beta\text{-Nb} \rightarrow \underset{> 10^{-30}\ \text{atm}\ O_2}{NbO_x} \rightarrow \underset{> 10^{-26}\ \text{atm}\ O_2}{Nb_2O_5}$$

Figure 3: Initial oxidation reactions of Nb-Zr alloys[31]

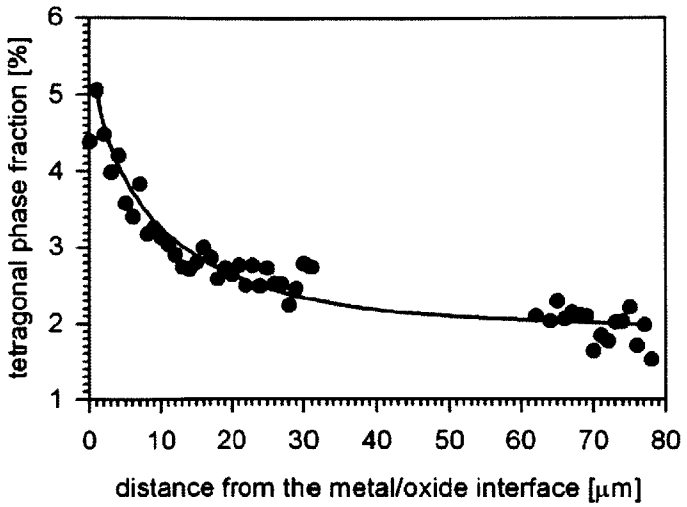

Figure 4: Tetragonal fraction in formed zirconium oxide as function of distance from interface[32]

A significant compressive stress forms in oxide in proximity to the metal/oxide interface due to lattice mismatch between metal and oxide [31]. Figure 5 shows compressive stress up to 5GPa as measured by Kim et al. More widely cited values for the stress formed near the interface is 0.5-1.0 GPa as shown on Figure 6 summarizing literature review conducted by Youssef and Yildiz. On the other hand, values measured by experimental techniques may underestimate local stresses, as they measure average over region which may include cracked or phase transitioned structures.

Orientation of the oxide and metal is crucial in computational work. Table 2 reviews experimental work on determining microstructure, and orientation of oxide formed in the corrosion process of Zr alloys. The work done by Arthur Motta's group provide a comprehensive information on existing oxide phases, and their orientations as shown in Figure 7. Monoclinic phase of ZrO2 is dominant away from the interface, while tetragonal phase is relatively stable in proximity to the interface. 001 orientation of t-ZrO2 proves to be dominant among other orientations as evidenced by the highest diffraction peak [8]. This work then focuses on 001 orientation of tetragonal zirconia in order to understand the effect of strain on defect energetics and equilibrium concentration.

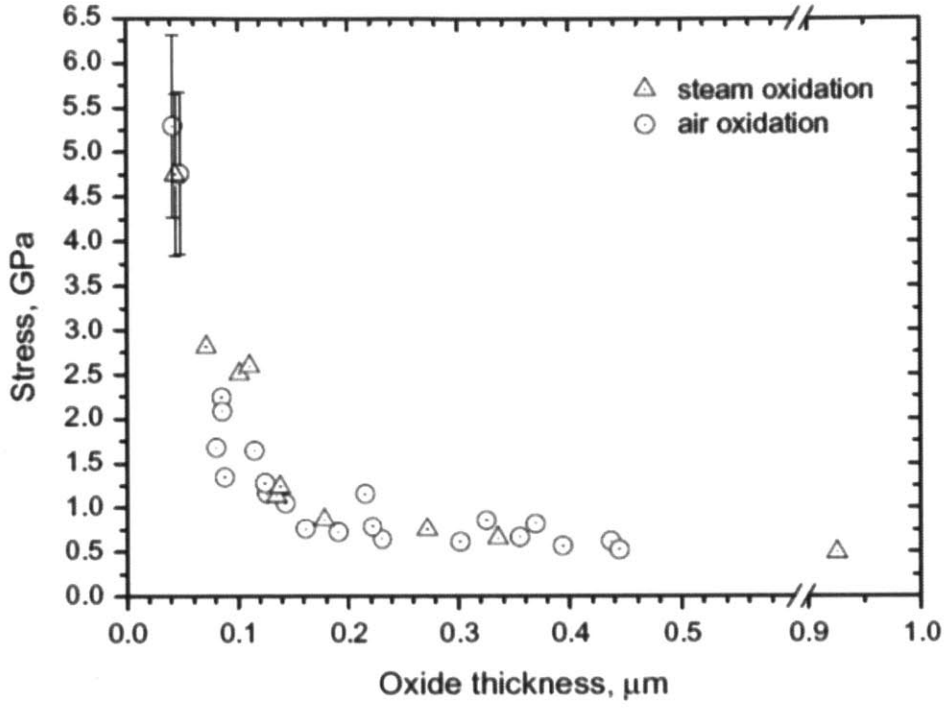

Figure 5: Stress formed in the oxide layer as function of distance from the metal/oxide interface[49]

Measurement technique	Specimen info.	Oxidizing conditions	Stress (GPa) vs. oxide thickness (μm)	
Deflection	Zr	Chem. agent/25 °C	0.2	1.2
XRD	Zr/Zry-2	O_2/500 °C	1.2	1.9
			(2.4)	(0.4)
Curvature	Zr/Zry-2	O_2/500–700 °C	0.6 (max.)	~3.0
Deflection	Zry-2	O_2/500 °C	1.7 (max.)	~3.8
Curvature	Zr/Zry-2	Steam/400 °C	0.5–1.3	Not available
	Zr–1Nb	Steam/550 °C	0.2–0.6	
Curvature	Zry-4(pickled)	Steam/400 °C	0.9–0.2	0.5–6
	Zry-4(polished)		0.6 (max.)	~3
XRD	Zr–1.2Sn–0.2Fe	Steam/420 °C	2.0–1.5	1.8–3.6
	Zr–0.5Sn–0.2Fe		1.8–1.5	1.4–2.6
XRD	Zry-4	Steam/400 °C	0.7–0.2	1.0–2.5
Raman	Zry-4	Water/360 °C	0.7–1.3	1.0–1.6
	Zr–1Nb–0.12O		0.8–1.5	1.0–2.5
Curvature	Zr	Steam and O_2/450 °C	5.1–0.5	0.1–1.0

Figure 6: Literature values of stress at the metal oxide interface due to lattice mismatch [35]

Author	Alloy	Oxide orientation	Stress
Motta et al [6]	ZIRLO	t-ZrO2,101 in bulk	
Hobbs et al [31]	Zr-2.6%Nb	t-ZrO2,111 in bulk	0.5-1.5GPa
Abolhassani et al [2]	Zircaloy-4	t-ZrO2,100	2.0-4.0GPa
Petigny et al [39]	Zr-1NbO	t-ZrO2,111	1.8GPa
Yilmazbayhan et al[9]	Zircaloy-4	t-ZrO2,101 at O/M ,101 in bulk	-
Yilmazbayhan et al[9]	Zr-2.5Nb	t-ZrO2,101 O/M interface	-
Preuss et al[32]	ZIRLO	t-ZrO2,101,Zr (1011)	1.5GPa
Preuss et al[32]	Zr-0.4Nb	t-ZrO2,101,1010 a-Zr	-
Ly et al[3]	Zircaloy-4	t-ZrO2,101	1.0GPa

Table 2: Review of experimental work on metal, oxide texture orientations in $\mathbf{ZrO_2}$

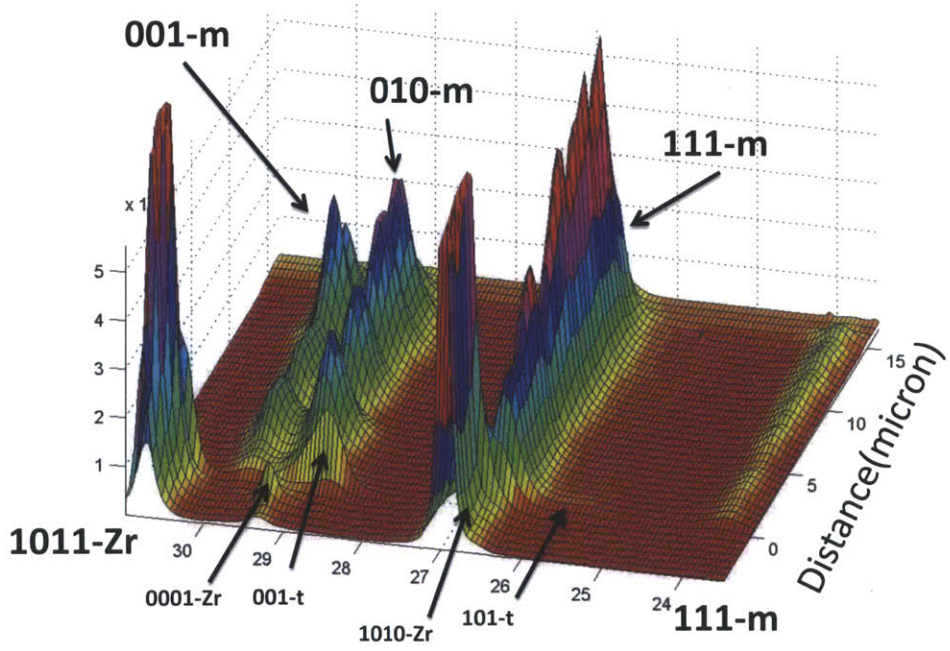

Figure 7: Crystal orientation map in proximity to metal/oxide interface[8]

Mechanistic corrosion kinetics experiments conducted in a simulated light reactor environment of 360°C steam for prolonged duration up to 200 days point to superior performance of these alloys compared to traditional alloys such as Zircaloy-4 and Zircaloy-2 as shown in Figure8 [8, 32]. The characteristic weight gain vs exposure time curve of Zr based alloys in reactor environment is given in Figure 9. The periodic discontinuous behavior of the weight gain curve is attributed to cracking of oxide layer due to stress followed by accelerated rate of corrosion. Effect of stress on defect formation in the oxide is also explored in this work.

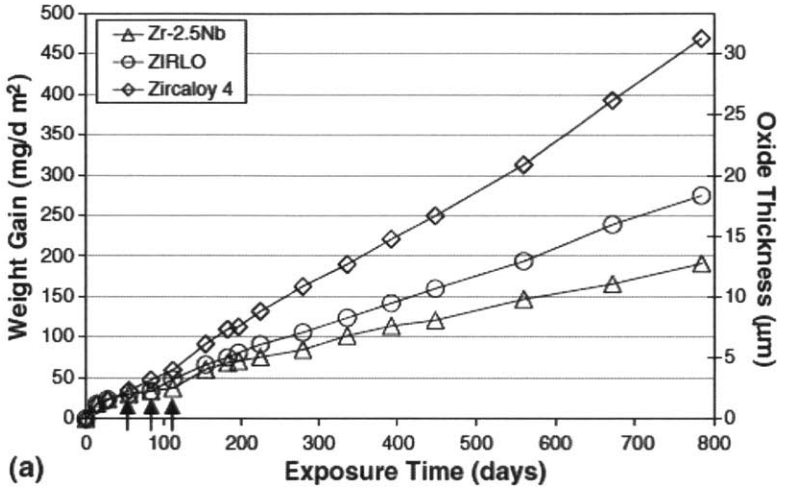

Figure 8: Formed oxide thickness for traditional and Nb containing alloys[8]

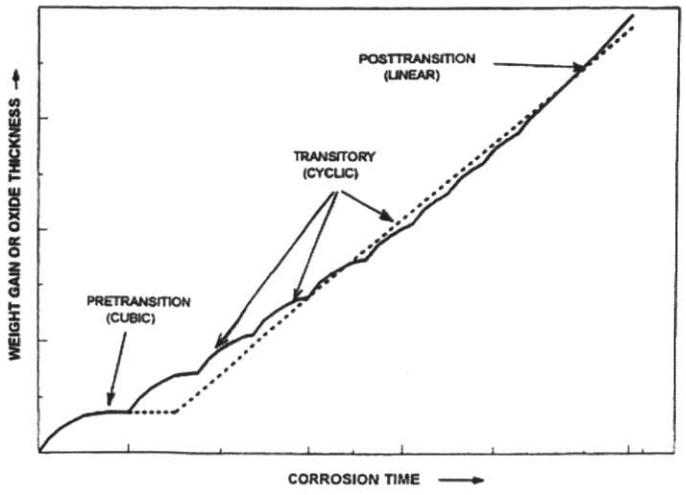

Figure 9: Characteristic weight gain curve for Zr based alloys[35]

1.3 Oxidation kinetics

The attempts to experimentally isolate the effect of Nb on corrosion kinetics have resulted in no clear conclusion. Yilmazbayhan et al conduct corrosion weight gain measurements on Zr based alloys with varying Nb content (0.4-2.5wt%Nb) while keeping other constituents constant, obtaining no clear correlation between them as in Figure 10 [8] which also agrees with the results of Yueh et al. On the other hand, Dali et al had observed a trend of deteriorated corrosion performance with higher Nb content [48]. Furthermore, Nb containing alloys have been shown to have inferior corrosion performance [20] in lithiated high temperature water[33] which can be encountered in reactor environment. Therefore, mechanistic corrosion kinetics experiments do not provide enough evidence to understand effect of Nb on corrosion of Zr alloys, and we aim to approach this problem by atomistic level first principle simulations.

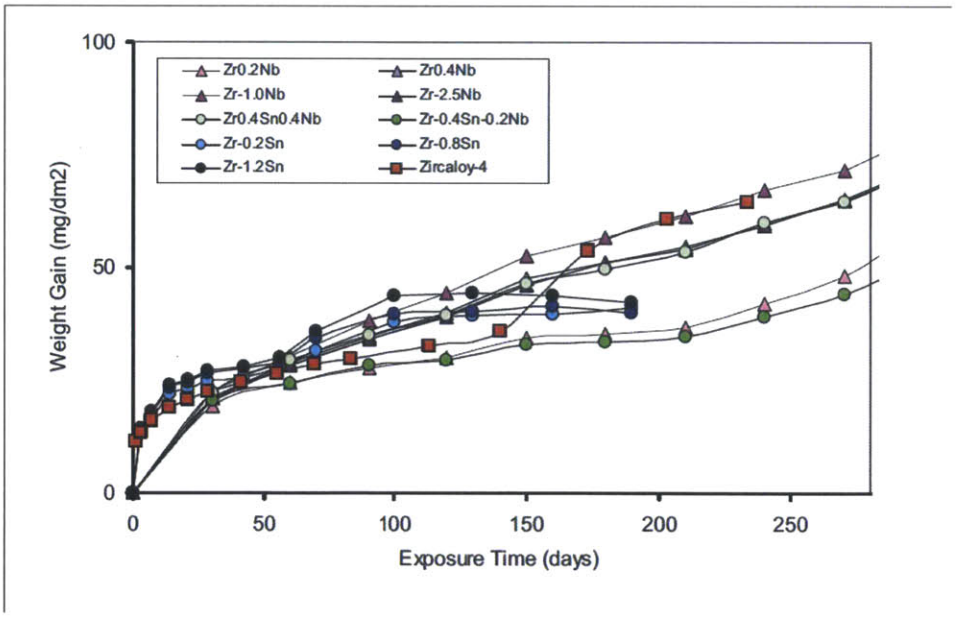

Figure 10: Corrosion rate of samples with varying Nb content[8]

Electrochemical process of oxide formation can be divided into several sub-processes first of which is dissociative water adsorption at water/oxide interface

$$\mathbf{H_2O + V_O^x \rightarrow ZrO_2 + 4H} \quad (1)$$

Oxygen and part of hydrogen created in this reaction then diffuse through the oxide layer to metal/oxide interface. Once the oxygen reaches metal, it dissolves into interstitial site to form solid solution. The positive charge transfer from the surface to the metal/oxide is compensated by electron conduction to the surface. The final stage is the formation of the zirconium oxide [35].

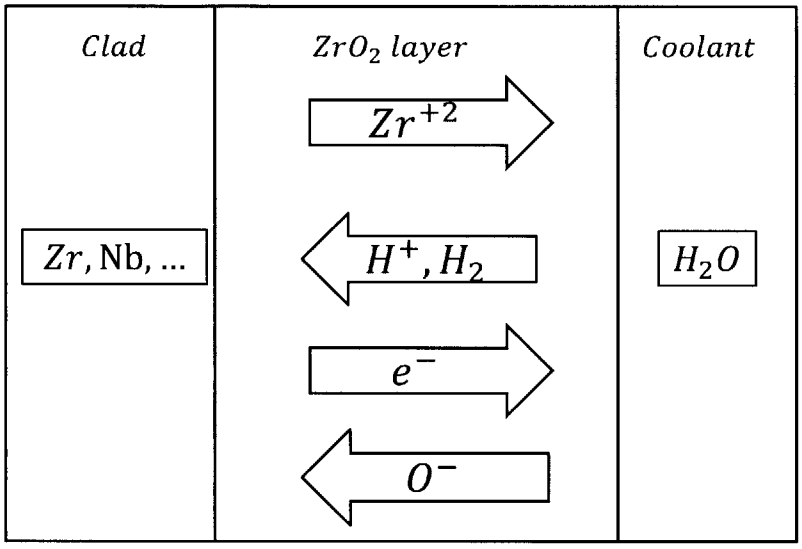

Figure 11: Transport processes participating in corrosion of zirconium alloy

Four of these sub-processes are considered rate limiting: hydrogen and oxygen diffusion through formed oxide layer to the metal, electron transport to water/oxide interface, and cation transport through oxide away from metal/oxide interface indicated by the schematic in Figure 11 [35]. We focus on oxygen diffusion, cationic diffusion, and electron conduction in this work.

Rate of transportation or the diffusion coefficient of species critical for corrosion can be

expressed as in Equation 2.

$$\mathbf{D} = \mathbf{D_v}[\mathbf{C}] \tag{2}$$

The two terms determining the diffusion rate of a species is the diffusivity or the mobility of that species $\mathbf{D_v}$, and the concentration of defects that mediate this diffusion process $[\mathbf{C}]$. The most direct way that an alloying element would affect the diffusion rate of a species is through the change in concentration of defects that mediate diffusion. Oxygen and cationic transport processes are mediated by oxygen point defects and cationic defects in the oxide layer [35]. We focused in this work on how Nb would affect the concentration of oxygen and cationic point defects thereby explaining the effect it would have on corrosion kinetics. We also want to quantify the effect of Nb on conduction band electron concentration that participates in electron transport process.

1.4 The objective and the structure of the thesis

As explained in previous subsection, defect concentration is critical in corrosion kinetics, and the objective of this thesis is to apply DFT informed framework to explain the role of Nb atom on defect concentration and corrosion kinetics in tetragonal zirconia. Our result indicates Nb slows down oxygen diffusion by decreasing concentration of available defect species but increases Zr ion diffusion coefficient by raising zirconium vacancy defect concentration. This effect implies better corrosion performance of Nb containing alloys compared to traditional alloys.

In order to arrive at this result, firstly, we studied Nb containing point defects systematically. We approached this by analyzing the structure, energetics, stability of Nb containing defects. We then integrated selected Nb containing defects into pure t-ZrO2 model in order to isolate the Nb effect. This part builds on earlier work done by Youssef and Yildiz [37]. They examined the native defects present in t-ZrO2 such as oxygen vacancy, oxygen interstitial,

zirconium vacancy and zirconium interstitial. In this work, we use these results and extend it to include Nb containing defects.

The way we observed Nb effect on equilibrium defect concentration is through constructing Kröger-Vink diagram which expresses concentration as a function of oxygen partial pressure in both Nb containing and pure t-ZrO2 cases. In order to construct Kröger-Vink diagram, DFT calculated defect formation energies are used. We did not include any charge state of a defect that is unbound or unstable, resulting in delocalization of electrons by DFT calculation, or too low in concentration in constructing the Kröger-Vink diagram. We also explained the observed linear behavior in Kröger-Vink diagram using simple mass action law in order to benchmark our model with simpler methods while proposing a charge compensation mechanism for Nb point defects.

As part of defect structure analysis, it was needed to identify the stable charge states of Nb in tetragonal ZrO2 as there is currently controversy about it. Experimental XANES K-edge measurement conducted by Froidevel et al concludes Nb charge state falls between +2 and +4, and +5 does not exist at all [5]. However, stable Nb+5 charge state even at the oxide/water interface is assumed by many authors [21, 31, 34]. The results of work presented in this thesis shows that all three charge states Nb+5, Nb+4, Nb+3 are stable and Nb+5 is dominant in concentration. We hope our work provides new insight into the problem of Nb charge state in zirconia.

Lastly, we want to identify the effect of compressive stress formed in the oxide due to lattice mismatch near the metal/oxide interface. The main reason of introducing compressive stress is to simulate tetragonal ZrO2 at the operating temperature of a reactor thereby bringing the temperature close to reality. Firstly, we want to see how stress affect the energetics, and structure of native and Nb containing defects. We perform this task by introducing artificial external stress by controlling compressive strain to all defect cells, and observed the effect it has on formation energy of important defects.

2 Computational Methods

2.1 Computational details

Energy and structural determination calculations are performed using Projector Augmented Wave (PAW) [14] in the Density Functional Theory (DFT) framework. Perdew Burke, and Ernzerhof (PBE) [28, 29] exchange correlation functional within GGA as implemented in Vienna Ab Initio Simulation Package (VASP) [23, 24, 26, 25] is employed. The adequacy of standard PBE functional to describe zirconia was discussed in our previous work [37, 36]. However, Niobium as a transition metal impurity in a material with a band gap can have multiple oxidation states. Standard DFT with its inherent self-interaction error may fail in properly localizing the d electrons needed to describe these multiple oxidation state. To overcome this issue we applied an intra-atomic onsite coulomb interaction term (the so-called U term) to the d electrons of Nb. We adapted a value of 1.5 eV for the U term as in [17]and employed the rotationally invariant version of DFT+U suggested by Dudarev et al [44]. In comparing PBE and PBE+U, we found both of them to stabilize only the charge states 3+,4+,5+ of Nb on a zirconium lattice site which is the most important Nb defect as we detail later. The main impact of the U term was found to increase the free energy of formation of the +5 charge state. In what follows we present results for PBE+U calculations, and in the Supplemental Material we provide the plain PBE results. Experimental values for the band gap ranges between 4.2 and 5.7eV[42, 15]. Monkhorst-Pack 2x2x2 k-point mesh is used for reciprocal space sampling. Plane wave expansion is cut-off at kinetic energy of 450 eV. Ionic relaxation was considered achieved when the forces on all ions were less than 0.01eV/Å. The convergence criterion for electronic free energy was set to $\mathbf{10^{-4}eV}$. The host T-ZrO2 simulation super cell of consists of 96 atoms, and point defect and defect complexes were added to the host super cell in their respective calculations. DFT calculations were performed in the dilute defect concentration limit and hence the super cell volume was fixed. Finite temperature effect is incorporated by including phonon contribution $\Delta\mathbf{F}_{\mathbf{vib}}^{\mathbf{solid}}$ to defect

formation free energy. ΔF_{vib}^{solid} is evaluated using VASP and software package Phonopy [4]at 1500K at which the tetragonal phase is stable [43]. The temperature is too high compared to the normal reactor operating temperature, but in absence of compressive stress to stabilize tetragonal phase, it would be unrealistic to simulate it at lower temperature as tetragonal phase would not stabilize there. In future, the effect from stress should be integrated to bring the simulation temperature closer to reality.

2.2 Defect structure analysis

In order to determine which charge states of Nb atom in certain defects take, we have adopted several different analytical approaches. Bader charge method is used to determine charge on an atom by processing results of DFT simulation [45, 16, 18]. The algorithm divides molecules into atoms based on definition of electron charge density, and zero flux surfaces, and provides a way of estimating charge localized on an atom. Secondly, electronic spin localization on an atom is determined using VASP in order to better resolve multiplet electron spin states. In addition to reporting spin values on each atom, spin density map is produced to visualize electronic localization. If a certain charge state of a defect or a defect complex resulted in delocalized electrons, we eliminated it from our consideration. Result of applying charge localization analysis to Nb substitutional defect is given in Section 2.5.2.

2.3 Thermodynamics of defects at T=0K

In this work, we adopt the Kröger-Vink notation for defects and defect complexes. For example $\mathbf{Nb_{Zr}}^{\cdot}$ represents a Nb atom sitting on Zr site (substituting) in the lattice with net charge of +1 compared to neutral undefected lattice. Sometimes we equivalently refer to this defect by the effective ionic charge of Nb+5. For defects complexes involving more than one point defects we separate them by a dash line as in $\mathbf{Nb_{Zr}}$–$\mathbf{V_O}$ representing oxygen vacancy bound to Nb substitutional point defect. More information on notation is given in

Appendix A.

Considered point defects in $\mathbf{t-ZrO_2}$ associated with niobium alloy are niobium interstitial $\mathbf{Nb_i}$, Nb substituting zirconium $\mathbf{Nb_{Zr}}$, and the defect complexes oxygen vacancy bound to substitutional niobium point defect $\mathbf{Nb_{Zr}-V_O}$, oxygen interstitial bound to substitutional niobium point defect $\mathbf{Nb_{Zr}-O_i}$. For $\mathbf{Nb_{Zr}}$ charge states +1, 0, -1 are found to be stable as more negatively charged defects result in de-localized electrons. Only octahedral site is considered for $\mathbf{Nb_i}$ with charge states from +1 to +5. $\mathbf{Nb_i}$ and defect complexes $\mathbf{Nb_{Zr}-V_O}$ and $\mathbf{Nb_{Zr}-O_i}$ are found to have higher formation energies and orders or magnitude lower concentration than $\mathbf{Nb_{Zr}}$ point defects, are therefore not discussed further in detail.

The system under investigation is modeled as a crystal of $\mathbf{t-ZrO_2}$ with defect, situated within a reservoir of oxygen. Free energy of formation of a defect within the host crystal is calculated by considering the insertion and removal of atoms from the crystal as formulated by Walle et al [12]. In the case of a point defect of niobium substituting zirconium, the formation energy of a charge q substitutional defect can be expressed as in Equation 3.

$$\Delta \mathbf{E^f_{Nb_{Zr}{}^q}} = \mathbf{E_{Nb_{Zr}{}^q}} - \mathbf{E^{DFT}_{bulk}} + \mu_{\mathbf{Zr}} - \mu_{\mathbf{Nb}} + \mathbf{q(E_{VBM}} + \mu_{\mathbf{F}}) + \mathbf{E_{MP}} \tag{3}$$

Where $\mathbf{E[Nb_{Zr}{}^q]}$ and $\mathbf{E^{DFT}_{ZrO_2}}$ are the coherent energies of defected and bulk super cells respectively. $\mathbf{E_{VBM}}$, $\mathbf{E_f}$ represent valence band maximum and the chemical potential of electrons. $\mathbf{E_{MP}}$ is a correction term for multiple electric interaction arising from applying periodic boundary condition for charged super cells [19].

Oxygen chemical potential is defined in terms of oxygen partial pressure $\mathbf{p_{O_2}}$ as in Equation 4 [37, 13]

$$\mu_{\mathbf{O_2}}(\mathbf{T}, \mathbf{p_{O_2}}) = \mathbf{E^{DFT}_{O_2}} + \mu^{\mathbf{0}}_{\mathbf{O_2}}(\mathbf{T}, \mathbf{P_0}) + \mathbf{k_B T ln}\left(\frac{\mathbf{p_{O_2}}}{\mathbf{p_0}}\right)(4) \tag{4}$$

Where $\mu^0_{\mathbf{O_2}}(\mathbf{T}, \mathbf{P})$ is chemical potential of oxygen gas at temperature T, pressure P_0 relative to 0K which can be looked up from thermo-chemical table [37, 1].

Chemical potentials $\mu_{\mathbf{Zr}}$, $\mu_{\mathbf{Nb}}$ depend on oxygen chemical potential in the system. Chemical potential of zirconium can be expressed as [37, 27]in Equation 5

$$\mu_{\mathbf{Zr}} = \mathbf{E}^{\mathbf{DFT}}_{\mathbf{ZrO_2}} - \mu_{\mathbf{O_2}} \tag{5}$$

where $\mathbf{E}^{\mathbf{DFT}}_{\mathbf{ZrO_2}}$ is the DFT calculated energy of a unit formula $\mathbf{ZrO_2}$. Hobbs et al constructed phase stability diagram for zirconium oxide and niobium oxide[31]. In their work, NbO is found to stabilize from metal Nb before $\mathbf{NbO_2}$, and $\mathbf{Nb_2O_5}$, and is therefore assumed to provide the limiting chemical potential value for μ_{Nb}. We can consequently express the chemical potential of niobium as in Equation 6

$$\mu_{\mathbf{Nb}} = \mathbf{E}^{\mathbf{DFT}}_{\mathbf{NbO}} - \frac{\mathbf{1}}{\mathbf{2}}\mu_{\mathbf{O_2}}(\mathbf{1atm}) \tag{6}$$

With $\mathbf{E}^{\mathbf{DFT}}_{\mathbf{NbO}}$ representing DFT calculated energy of NbO unit formula. This chemical potential value for niobium is kept constant throughout this work.

2.4 Thermodynamics of native defects

2.4.1 Oxygen vacancy

Oxygen vacancies are created by removing an oxygen atom from a simulation cell. Therefore the formation energy of this defect has to be the difference between the DFT calculated coherent energies of undefected and defected cells offset by the energy corresponding to the removed oxygen atom which is the oxygen chemical potential. For charged oxygen vacancies, energy that was carried by removed or added electrons have to be considered in the formation energy calculations as shown in Equation 7.

$$\Delta\mathbf{E}^{\mathbf{f}}_{\mathbf{V_O{}^q}} = \mathbf{E}_{\mathbf{V_O{}^q}} - \mathbf{E}^{\mathbf{DFT}}_{\mathbf{perfect}} + \mu_{\mathbf{O}} + \mathbf{q}(\mathbf{E_{VBM}} + \mu_{\mathbf{F}}) + \mathbf{E_{MP}} \tag{7}$$

2.4.2 Oxygen interstitial

Oxygen interstitials are created by adding an oxygen atom from a simulation cell. Therefore the formation energy of this defect has to be the difference between the DFT calculated coherent energies of undefected and defected cells offset by the energy corresponding to the added oxygen atom which is the oxygen chemical potential. For charged oxygen interstitials, energy that was carried by removed or added electrons have to be considered in the formation energy calculations as shown in Equation 8.

$$\Delta \mathbf{E}^{\mathbf{f}}_{\mathbf{O_i}^{\mathbf{q}}} = \mathbf{E}_{\mathbf{O_i}^{\mathbf{q}}} - \mathbf{E}^{\mathbf{DFT}}_{\mathbf{perfect}} - \mu_{\mathbf{O}} + \mathbf{q}(\mathbf{E}_{\mathbf{VBM}} + \mu_{\mathbf{F}}) + \mathbf{E}_{\mathbf{MP}} \tag{8}$$

2.4.3 Zr vacancy

Zirconium vacancies are created by removing a Zr atom from a simulation cell. Therefore the formation energy of this defect has to be the difference between the DFT calculated coherent energies of undefected and defected cells offset by the energy corresponding to the removed Zr atom which is calculated from the oxygen chemical potential. For charged Zr vacancies, energy that was carried by removed or added electrons have to be considered in the formation energy calculations as shown in Equation 9.

$$\Delta \mathbf{E}^{\mathbf{f}}_{\mathbf{V_{Zr}}^{\mathbf{q}}} = \mathbf{E}_{\mathbf{V_{Zr}}^{\mathbf{q}}} - \mathbf{E}^{\mathbf{DFT}}_{\mathbf{perfect}} + \mu_{\mathbf{Zr}} + \mathbf{q}(\mathbf{E}_{\mathbf{VBM}} + \mu_{\mathbf{F}}) + \mathbf{E}_{\mathbf{MP}} \tag{9}$$

2.4.4 Zr interstitial

Zirconium interstitials are created by adding an oxygen atom from a simulation cell. Therefore the formation energy of this defect has to be the difference between the DFT calculated coherent energies of undefected and defected cells offset by the energy corresponding to the added Zr atom which is calculated from the oxygen chemical potential. For charged oxygen interstitials, energy that was carried by removed or added electrons have to be considered in

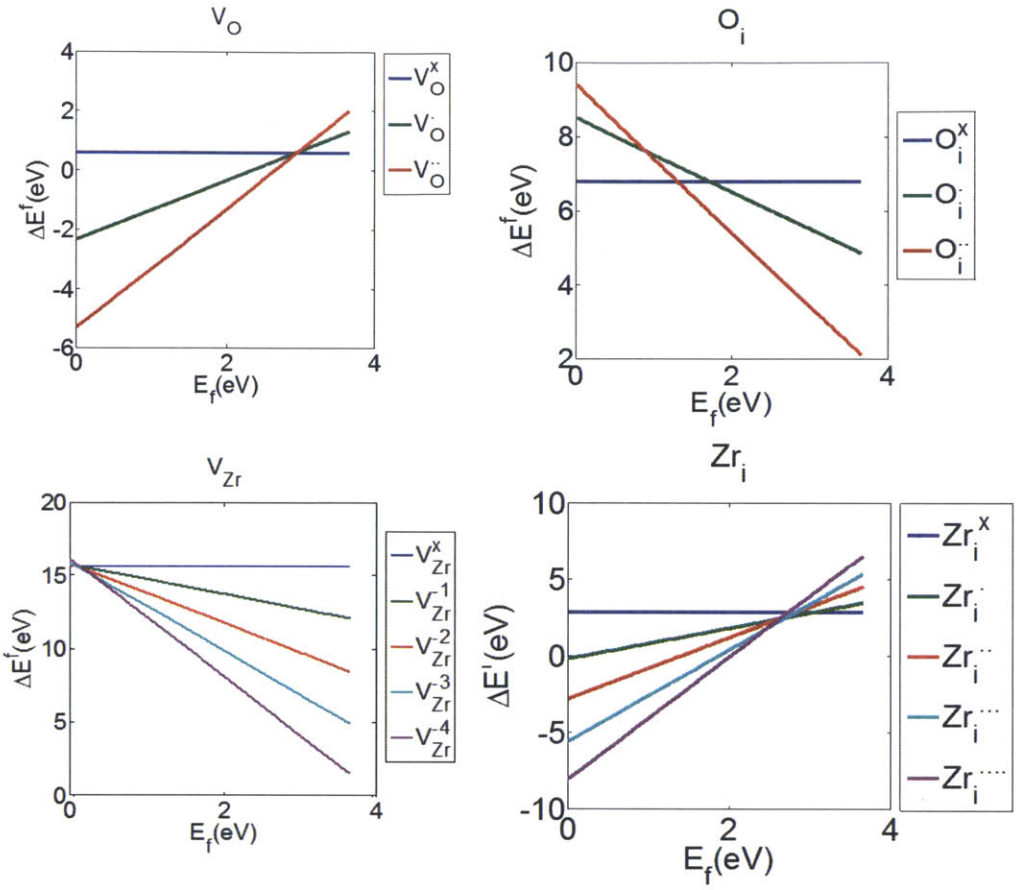

Figure 12: Formation energy of native defects as function of chemical potential of electrons, pO2 level corresponding to oxygen poor condition which may occur near metal/oxide interface with $\mathbf{pO_2 = 10^{-20}atm}$.

the formation energy calculations as shown in Equation 10.

$$\Delta \mathbf{E^f_{Zr_i{}^q}} = \mathbf{E_{Zr_i{}^q}} - \mathbf{E^{DFT}_{perfect}} - \mu_{\mathbf{Zr}} + \mathbf{q(E_{VBM} + \mu_F)} + \mathbf{E_{MP}} \tag{10}$$

The formation energy for four native defects as function of chemical potential of electrons is presented in Figure 13

2.5 Defects involving Niobium

When alloying element is introduced to the system, charge equilibrium can change. In particular, in our system of interest, Nb occurs in wt 2.5% concentration potentially participating in formation of point defects and defect complexes. This section examines energetics and electronic structure of Nb substitutional point defect and other associated defect complexes. Formation free energies of all considered defects ($\mathbf{Nb_{Zr}}, \mathbf{Nb_i}$, $\mathbf{Nb_{Zr} - V_O}$, $\mathbf{Nb_{Zr} - O_i}$) are calculated from DFT computations. Results from later analysis indicate that $\mathbf{Nb_{Zr}}$is the highest concentration defect among others. Therefore this section will have heavy focus on $\mathbf{Nb_{Zr}}$, and provide overview of analysis conducted on Niobium interstitial and defect complexes.

2.5.1 Formation energy

Nb substitutional point defects are created by replacing a lattice Zr atom by an alloying Nb atom in a simulation cell. Therefore the formation energy of this defect has to be the difference between the DFT calculated coherent energies of undefected and defected cells offset by the energy corresponding to the removed Zr atom, and added Nb atom. The chemical potential of Zr and Nb are calculated from the oxygen chemical potential in Equations 5,6 respectively. For charged oxygen interstitials, energy that was carried by removed or added electrons have to be considered in the formation energy calculations as shown in Equation 11.

$$\mathbf{\Delta E^f_{Nb_{Zr}{}^q} = E_{Nb_{Zr}{}^q} - E^{DFT}_{perfect} + \mu_{Zr} - \mu_{Nb} + q(E_{VBM} + \mu_F) + E_{MP}} \tag{11}$$

The resulting -U plot showing the lowest formation energy charge states is shown in Figure 13.

For Nb_{Zr} point defect, charge localization analysis is performed on DFT computed defect electronic structure in order to identify stable charge states. Consequently, formation ener-

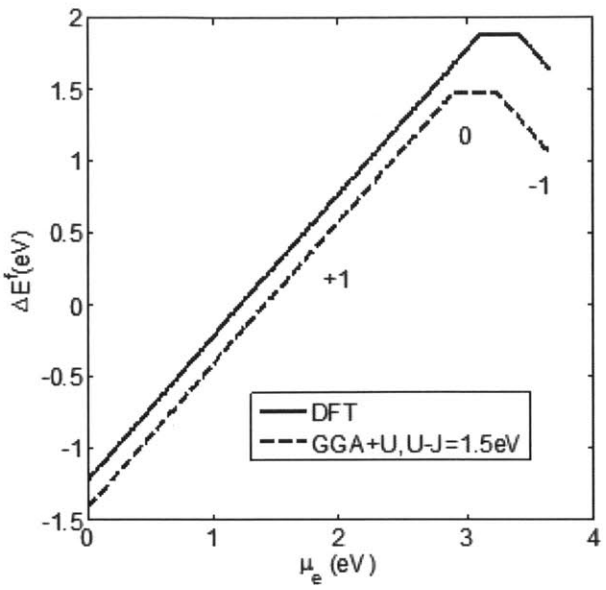

Figure 13: Formation energy of Nb substitutional point defect

gies of all considered defects ($\mathbf{Nb_{Zr}}, \mathbf{Nb_i}$, $\mathbf{Nb_{Zr} - V_O}$, $\mathbf{Nb_{Zr} - O_i}$) are calculated from DFT computations. Kröger-Vink diagram is constructed using DFT calculated defect energies. Details of these analyses are presented in the following sections.

In addition to $\mathbf{Nb_{Zr}}$ point defect, we have also considered Niobium interstitial and defect complexes involving Nb. These defects turned out to have negligible concentration compared to $\mathbf{Nb_{Zr}}$ point defect after constructing Kroger-Vink diagram. However, we provide overview of the approach and results. The formation free energy of Niobium interstitial $\mathbf{Nb_i}$ is defined as in Equation 12.

$$\Delta \mathbf{E^f_{Nb_i{}^q}} = \mathbf{E_{Nb_i{}^q}} - \mathbf{E^{DFT}_{perfect}} - \mu_{\mathbf{Nb}} + \mathbf{q}(\mathbf{E_{VBM}} + \mu_{\mathbf{F}}) + \mathbf{E_{MP}} \tag{12}$$

For oxygen vacancy bound to Nb substitutional defect, $\mathbf{Nb_{Zr} - V_O}$, the formation free energy is defined as in Equation 13

$$\Delta \mathbf{E^f_{Nb_{Zr}-V_O{}^q}} = \mathbf{E_{Nb_{Zr}-V_O{}^q}} - \mathbf{E^{DFT}_{perfect}} + \mu_{\mathbf{Zr}} - \mu_{\mathbf{Nb}} + \mu_{\mathbf{O}} + \mathbf{q}(\mathbf{E_{VBM}} + \mu_{\mathbf{F}}) + \mathbf{E_{MP}} \tag{13}$$

For oxygen vacancy bound to Nb substitutional defect, $Nb_{Zr} - O_i$, the formation free energy is defined as in Equation 14

$$\Delta \mathbf{E}^{\mathbf{f}}_{\mathbf{Nb_{Zr}-O_i{}^q}} = \mathbf{E}_{\mathbf{Nb_{Zr}-O_i{}^q}} - \mathbf{E}^{\mathbf{DFT}}_{\mathbf{perfect}} + \mu_{\mathbf{Zr}} - \mu_{\mathbf{Nb}} - \mu_{\mathbf{O}} + \mathbf{q}(\mathbf{E}_{\mathbf{VBM}} + \mu_{\mathbf{F}}) + \mathbf{E}_{\mathbf{MP}} \quad (14)$$

We plot the resulting free energy of formation as a function of chemical potential of electrons in Figure 14.

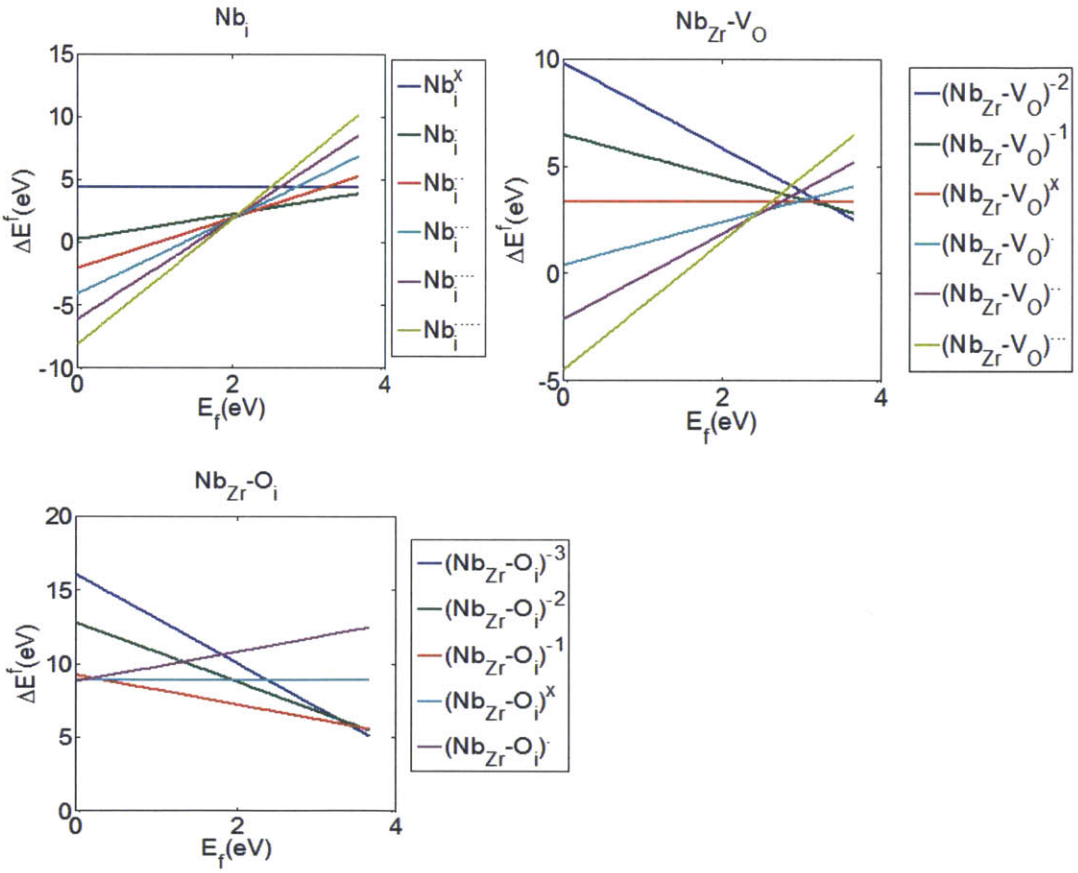

Figure 14: Formation energies of Niobium interstitial, and defect complexes at oxygen poor condition with $\mathbf{pO_2 = 10^{-20} atm}$.

Defect charge	$Nb_{Zr}^{''}$	$Nb_{Zr}^{'}$	Nb_{Zr}^{x}	$Nb_{Zr}^{\cdot}$
Cell charge (e)	-2	-1	0	+1
Bader charge on Nb (e)	2.0	2.0	2.3	2.6
Spin on Nb/ net cell spin (μ_B)	1.6/1.3	1.6/1.8	0.8/0.9	0/0
Inferred charge assignment	Delocalized e	Nb+3	Nb+4	Nb+5

Table 3: Cell charge, Bader charge on Nb defect, spin on Nb defect/net cell spin. Charge assignments based on these analysis is also presented

2.5.2 Defect structure

Analysis on the charge localization on Nb substitutional point defects is performed in this section. Electrons are artificially added and removed from the DFT simulation super cell of Nb_{Zr} point defect to simulate various charged defects. To start, an electron was removed from neutral point defect super cell to simulate +1 charged point defect which is theoretically the most positive possible state. Electrons were then added sequentially until the point of delocalization. Electron localization on Nb atom is necessary for stability of defect and analysis was performed at each charge as shown Figure 15, and Table 3. The charge states of Nb which resulted in delocalized electrons were considered not to exist. Table 3 provides the net spin density for the three Nb substitutional defects for which charge localization was observed as well as Bader charges on the defect. Since Nb+3 and less positive charge states result in delocalization they are neither further discussed nor integrated into the construction of Kröger Vink diagram. Delocalization is evidenced by almost negligible Bader charge on Nb when transitioning from Nb+3 to Nb+2. Incremental change in Bader charge on Nb, as electrons added to the cell, suggests localization of Nb resulting in reduced net charge on it. Electronic spin density map was produced in all defect charge states Nb+3, Nb+4, Nb+5 in Figures 15B and 15C, and localized electrons on the Nb defect are visible from electron density isosurface.

In Figure 15, spin density map of a defected unit cell represented. Green represents Zr atoms, blue Nb atoms, gray spin 0.01e/$\mathbf{\AA^3}$ isosurface. On $\mathbf{(A)Nb_{Zr}^{\cdot}(B)Nb_{Zr}^{x}(C)Nb_{Zr}^{\cdot}}$ unit cells are represented. Charge localization on defect is evident in (B) and (C) making the effective

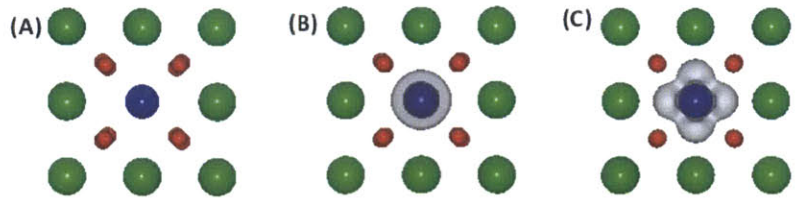

Figure 15: Spin density map of a defected unit cell. Green represents Zr atoms, blue Nb atoms.

charge state of Nb atom +4 and +3. Unit cell lattice constant is 5.14 **Å** In figures. 15B and 15C one can clearly see localized electrons on the Nb defect. From DFT based charge localization analysis as well as Bader charge analysis, we can conclude that Nb charge states +3, +4, +5 or -1, 0, +1 defect charges can exist in $\mathbf{Nb_{Zr}}$ point defect. More negative defect charges result in delocalized electrons and are not included in further analysis.

GGA+U computations resulted in the same outcome as Nb+2 charge state resulted in delocalized electron, and Nb+5,Nb+4,Nb+3 charge states were found to be stable. However, energy calculations using DFT+U resulted in different values from DFT, and Kröger-Vink diagram constructed by using DFT+U values is presented in due section.

The resulting formation energy of $\mathbf{Nb_{Zr}}$ defect at T=0K, under assumed oxygen rich condition, as a function of chemical potential of electrons calculated from Equation 3. Kinks in the line represent transitions into different defect charge states. $\mathbf{Nb_{Zr}^{\cdot}}$ is dominant over a wide range of possible electron chemical potential over other considered different charged defects, and is given in Figure 13. Other defect charges were ignored as our simulation resulted in delocalization of electrons. Results of GGA+U calculations are also presented in the same plot. DFT+U results in slightly higher formation energy for $\mathbf{Nb_{Zr}}$ defect which translates into significantly different Kröger-Vink diagram from DFT as discussed in next section. Charge states with the lowest formation energy at each chemical potential of electrons is represented with a line in Figure 13. +1 charged Nb point defect which corresponds to Nb+5 charge state is found to occupy greater portion of possible chemical potential of electrons range than the other two charge states. This finding is also confirmed in Kröger-

Vink diagram where $\mathbf{Nb_{Zr}}$ was found to exist in orders of magnitude higher concentration than $\mathbf{Nb^{x}_{Zr}}$,$\mathbf{Nb^{'}_{Zr}}$.

2.5.3 Stability

We define binding energy for a defect complex as a quantity to measure stability with respect to dissociation into its constituents. For Nb_{Zr} point defect, we determine its binding energy with respect to the dissociation into a zirconium vacancy and niobium interstitial. Binding energy for $\mathbf{Nb_{Zr}}$ q is defined as in Equation 15.

$$\mathbf{E_{bind}} = \mathbf{max}\left[\mathbf{E^{DFT}_{Nb_{Zr}{}^{q}}} - \left(\mathbf{E^{DFT}_{V_{Zr}{}^{Q}}} + \mathbf{E^{DFT}_{Nb_{i}^{q-Q}}}\right)\right] \tag{15}$$

where Q represents the charge of zirconium vacancy point defect which has to be compensated by charge of $\mathbf{Nb_i}$. All possible charge distributions i.e values of Q for each $\mathbf{Nb_{Zr}{}^{q}}$ are examined, and the dissociation with the most positive binding energy is presented in Table 4. In our definition, negative binding energy corresponds to bound state. So, the negative binding energies found from this analysis indicate that $\mathbf{Nb_{Zr}}$ point defect is stable with respect to the dissociation into $\mathbf{V_{Zr}}$ and Nb_i. Similar binding energy analysis was conducted to evaluate stability of all defect complexes involving Nb ($\mathbf{Nb_{Zr}}$, $\mathbf{Nb_i}$,$\mathbf{Nb_{Zr}-V_O}$, $\mathbf{Nb_{Zr}-O_i}$). For each complex we eliminated the charge states with positive binding energy and excluded from constructing Kröger Vink diagram.

For Nb substitutional point defect $\mathbf{Nb_{Zr}}$, the dissociation path with respect to which the binding energy is defined is given in Equation 16, and binding energies for possible dissociation charge assignments are given in Table 9.

$$\mathbf{Nb_{Zr}} \rightarrow \mathbf{Nb_i} + \mathbf{V_{Zr}} \tag{16}$$

For oxygen vacancy bound to Nb substitutional point defect $\mathbf{Nb_{Zr}} - \mathbf{V_O}$, we consider two possible dissociation pathways in which the binding energy is defined as given in Equation

Nb_{Zr}	-1	0	+1
E_{bind}	-5.2eV	-6.6eV	-7.7eV
Nb_i	+3	+4	+5
V_{Zr}	-4	-4	-4

Table 4: Binding energies of Nb_{Zr} defects with different charges. The charges of V_{Zr} and Nb_i that result in the least bound dissociation path are also presented

	Nb''_{Zr}	Nb'_{Zr}	Nb^x_{Zr}	$Nb^{\cdot}_{Zr}$	$Nb^{\cdot\cdot}_{Zr}$	$Nb^{\cdot\cdot\cdot}_{Zr}$
$V^{\cdot\cdot}_O$	-2.1	-1.1	-0.3	0.5	-	-
$V^{\cdot}_O$	-2.1	-1.1	-0.7	-0.1	-2.70	-
V^x_O	-1.6	-1.0	-2.2	-0.5	-3.3	-5.7

Table 5: Binding energies of $Nb_{Zr} - V_O$ defect complex with different charges. Blue is +3, pink is +2,green is +1, yellow is neutral, light blue is -1, red is -1 charged defect complex.

17, and binding energies for possible dissociation charge assignments are given in Tables 6,5.

$$\begin{cases} Nb_{Zr} - V_O \rightarrow Nb_{Zr} + V_O \\ Nb_{Zr} - V_O \rightarrow Nb_i + V_{Zr} + V_O \end{cases} \tag{17}$$

Similarly,for oxygen vacancy bound to Nb substitutional point defect $Nb_{Zr} - O_i$, we consider two possible dissociation pathways in which the binding energy is defined as given in Equation 34, and binding energies for possible dissociation charge assignments are given in Tables 8,7.

$$\begin{cases} Nb_{Zr} - O_i \rightarrow Nb_{Zr} + O_i \\ Nb_{Zr} - O_i \rightarrow Nb_i + V_{Zr} + O_i \end{cases} \tag{18}$$

2.6 Finite temperature effect

The DFT calculated energy values are taken at T=0K may result in incorrect qualitative and quantitative conclusions[27, 37]. In order to include temperature effect into our model, we start with defining the Gibbs free energy of defect formation as in Equation 19[37]

$$\mathbf{G^f_{D,q} = \Delta E^{solid}_{potential} + \Delta F^{solid}_{vib} - T\Delta S^{solid}_{e} + P\Delta V \pm \mu_D} \tag{19}$$

	V_O^x					
	Nb_i^x	$Nb_i^{\cdot}$	$Nb_i^{\cdot\cdot}$	$Nb_i^{\cdot\cdot\cdot}$	$Nb_i^{\cdot\cdot\cdot\cdot}$	$Nb_i^{\cdot\cdot\cdot\cdot\cdot}$
V_{Zr}^x	-17.3	-16.2	-16.4	-16.7		
$V_{Zr}^{'}$	-14.3	13.3	-13.9	-14.4	-14.8	
$V_{Zr}^{''}$	-11.0	-10.2	-11.0	-11.9	-12.4	-12.8
$V_{Zr}^{'''}$	-	-6.9	-8.0	-9.0	-10.0	-10.5
$V_{Zr}^{''''}$	-	-	-4.9	-6.2	-7.3	-8.2
	$V_O^{\cdot}$					
	Nb_i^x	$Nb_i^{\cdot}$	$Nb_i^{\cdot\cdot}$	$Nb_i^{\cdot\cdot\cdot}$	$Nb_i^{\cdot\cdot\cdot\cdot}$	$Nb_i^{\cdot\cdot\cdot\cdot\cdot}$
V_{Zr}^x	-17.4	-15.8	-15.8	-	-	-
$V_{Zr}^{'}$	-14.4	-13.3	-13.5	-13.8	-	-
$V_{Zr}^{''}$	-11.4	-10.4	-11.0	-11.5	-11.9	-
$V_{Zr}^{'''}$	-8.1	-7.3	-8.1	-9.0	-9.6	-10.0
$V_{Zr}^{''''}$	-	-4.2	-5.3	-6.3	-7.3	-7.8
	$V_O^{\cdot\cdot}$					
	Nb_i^x	$Nb_i^{\cdot}$	$Nb_i^{\cdot\cdot}$	$Nb_i^{\cdot\cdot\cdot}$	$Nb_i^{\cdot\cdot\cdot\cdot}$	$Nb_i^{\cdot\cdot\cdot\cdot\cdot}$
V_{Zr}^x	-16.9	-15.2	-	-	-	-
$V_{Zr}^{'}$	-14.4	-12.9	-12.9	-	-	-
$V_{Zr}^{''}$	-11.5	-10.3	-10.6	-10.9	-	-
$V_{Zr}^{'''}$	-8.5	-7.5	-8.1	-8.6	-9.0	-
$V_{Zr}^{''''}$	-5.4	-4.6	-5.4	-6.3	-6.9	-7.2

Table 6: Binding energies of $Nb_{Zr} - V_O$ defect complex with respect to decomposition into three defect species with different charges. Blue is +3, pink is +2,green is +1, yellow is neutral, light blue is -1, red is -1 charged defect complex.

	$Nb_{Zr}^{''}$	$Nb_{Zr}^{'}$	Nb_{Zr}^x	$Nb_{Zr}^{\cdot}$	$Nb_{Zr}^{\cdot\cdot}$	$Nb_{Zr}^{\cdot\cdot\cdot}$
O_i^x	-4.8	-4.4	-1.3	1.7	-	-
$O_i^{'}$	-3.3	-2.5	-2.7	0.1	-0.2	-
$O_i^{''}$	-	-0.2	-0.0	-0.5	-1.0	-1.1

Table 7: Binding energies of $Nb_{Zr} - O_i$ defect complex with different charges. Green is +1, yellow is neutral, light blue is -1, red is -1, black is -2 charged defect complex.

	O_i^x					
	Nb_i^x	$Nb_i^{\cdot}$	$Nb_i^{\cdot\cdot}$	$Nb_i^{\cdot\cdot\cdot}$	$Nb_i^{\cdot\cdot\cdot\cdot}$	$Nb_i^{\cdot\cdot\cdot\cdot\cdot}$
V_{Zr}^x	-18.0	-13.9				
$V_{Zr}^{'}$	-17.7	13.9	-11.7			
$V_{Zr}^{''}$	-14.2	-13.6	-11.6	-9.7		
$V_{Zr}^{'''}$	-11.0	-10.1	-11.4	-9.7	-7.8	
$V_{Zr}^{''''}$	-	-7.1	-8.1	-9.6	-7.9	-6.0
	$O_i^{'}$					
	Nb_i^x	$Nb_i^{\cdot}$	$Nb_i^{\cdot\cdot}$	$Nb_i^{\cdot\cdot\cdot}$	$Nb_i^{\cdot\cdot\cdot\cdot}$	$Nb_i^{\cdot\cdot\cdot\cdot\cdot}$
V_{Zr}^x	-19.4	-15.6	-13.3			
$V_{Zr}^{'}$	-15.9	-15.3	-13.3	-11.4		
$V_{Zr}^{''}$	-12.6	-11.8	-13.0	-11.3	-9.4	
$V_{Zr}^{'''}$		-8.6	-9.6	-11.1	-9.4	-7.5
$V_{Zr}^{''''}$			-6.5	-7.8	-9.3	-7.6
	$O_i^{''}$					
	Nb_i^x	$Nb_i^{\cdot}$	$Nb_i^{\cdot\cdot}$	$Nb_i^{\cdot\cdot\cdot}$	$Nb_i^{\cdot\cdot\cdot\cdot}$	$Nb_i^{\cdot\cdot\cdot\cdot\cdot}$
V_{Zr}^x	-16.7	-9.6	-14.2	-12.2		
$V_{Zr}^{'}$	-13.5	-12.6	-9.6	-12.2	-10.2	
$V_{Zr}^{''}$		-9.4	-10.3	-9.6	-10.2	-8.3
$V_{Zr}^{'''}$			-7.2	-8.4	-9.6	-8.3
$V_{Zr}^{''''}$				-5.4	-6.6	-9.6

Table 8: Binding energies of $Nb_{Zr} - O_i$ defect complex with respect to decomposition into three defect species with different charges. Blue is +3, pink is +2,green is +1, yellow is neutral, light blue is -1, red is -1 charged defect complex.

	Nb_i^x	$Nb_i^{\cdot}$	$Nb_i^{\cdot\cdot}$	$Nb_i^{\cdot\cdot\cdot}$	$Nb_i^{\cdot\cdot\cdot\cdot}$	$Nb_i^{\cdot\cdot\cdot\cdot\cdot}$
V_{Zr}^x	-16.7	-15.7	-13.1	-11.1	-	-
$V_{Zr}^{'}$	-13.3	-12.6	-13.4	-11.1	-9.1	-
$V_{Zr}^{''}$	-9.3	-9.2	-10.3	-11.4	-9.2	-7.1
$V_{Zr}^{'''}$	-	-5.3	-7.0	-8.4	-9.5	-7.2
$V_{Zr}^{''''}$	-	-	-3.2	-5.2	-6.6	-7.7

Table 9: Binding energies of Nb_{Zr} point defect with respect to decomposition into Nb interstitial and Zr vacancy with different charges. Blue is +3, pink is +2, green is +1, yellow is neutral, light blue is -1, red is -1 charged defect complex.

where $\mathbf{\Delta E^{solid}_{potential}}$ is the difference in potential energy between defected and undefected cell. $\mathbf{\Delta F^{solid}_{vib}}$ is the contribution from phonons to free energy of formation, and $\mathbf{\Delta S^{solid}_{e}}$ represents the change solid electronic entropy. In this work, electronic entropy term is not taken into account nor is the volume change ΔV due to dilute nature of defects. The contribution from the electronic entropy has been shown to be not as significant as the phonons. The contribution from the lattice vibration or the phonon contribution is calculated by Equation 20.

$$\mathbf{F^{solid}_{vib}} = \mathbf{N k_B T} \int_0^\infty \mathbf{g}(\omega) \ln \left[\mathbf{2 Sinh} \left(\frac{\hbar \omega}{\mathbf{2 k_B T}} \right) \right] \mathbf{d}\omega \tag{20}$$

where $g(\omega)$is the Density of states for the phonons. In our simulation, to calculate $\mathbf{\Delta F^{solid}_{vib}}$, the elastic constants of crystall vibration are first calculated using VASP, and phonon vibrational frequency calculations are implemented using software package Phonopy [4] at 1500K at which the tetragonal phase is stable [30]. The unrealistically high temperature is later relaxed in our work by including the effect of stress on defect formation in experimental temperature range.

3 Kröger-Vink diagram

3.1 Constructing Kröger-Vink diagram

This work is an extension to earlier work Youssef and Yildiz[37] have performed on the defect thermodynamics in pure $\mathbf{t-ZrO_2}$ including the construction of Kröger-Vink (Brouwer) diagram. In pure $\mathbf{t-ZrO_2}$, only native point defects such as $\mathbf{V_O}$, $\mathbf{O_i}$, $\mathbf{V_{Zr}}$, $\mathbf{Zr_i}$ need to be considered. This work extends the previous work by adding Nb associated defects which might arise from the presence of the alloying niobium, and aims to understand its effect on the equilibrium defect concentrations. As the concentration of Nb is very low, we assume thermodynamic equilibrium. However, Nb can impact the concentration of native defects through charge compensation. Charge neutrality condition in any crystal defect system can be written as in Equation 21

$$\sum \mathbf{q}[\mathbf{D_X^q}] + \mathbf{p_v} - \mathbf{n_c} = \mathbf{0} \tag{21}$$

where $[\mathbf{D_X^q}]$denotes the concentration of a defect of type X and charge q, which is summed over all defect types and charges.$\mathbf{p_v}, \mathbf{n_c}$ represent hole and conduction band electron concentrations respectively. We follow the derivation by Kasamatsu et al [43] in calculating defect concentration as in Equation 22

$$[\mathbf{D_X^q}] = \frac{\mathbf{n_D exp}\left(-\frac{\mathbf{\Delta E^f_{X,q}}}{\mathbf{k_B T}}\right)}{\mathbf{1} + \sum_{\mathbf{q'}} \mathbf{exp}\left(-\frac{\mathbf{\Delta E^f_{X,q'}}}{\mathbf{k_B T}}\right)} \tag{22}$$

where $\mathbf{n_D}$ denotes the number of possible sites for a given defect. Concentration of electrons and holes can be calculated applying Fermi-Dirac distribution as in Equation 23,24[37, 7].

$$\mathbf{n_c} = \int_{\mathbf{E_{CBM}}}^{\infty} \mathbf{g_c(E)} \frac{\mathbf{dE}}{\mathbf{1} + \mathbf{exp}\left(\frac{\mathbf{E-E_f}}{\mathbf{k_B T}}\right)} \tag{23}$$

$$\mathbf{n_c} = \int_{-\infty}^{\mathbf{E_{VBM}}} \mathbf{g_v(E)} \frac{\mathbf{dE}}{\mathbf{1 + exp\left(\frac{E_f - E}{k_B T}\right)}} \tag{24}$$

$\mathbf{g_c(E)}$and $\mathbf{g_v(E)}$ are the Density of States (DOS) in conduction and valence band respectively. It is widely known that DFT calculated band gaps are usually inaccurate[13]. Therefore we adopt an approach implemented in our earlier work by artificially elongating DFT calculated band gap 3.9eV for pure $\mathbf{ZrO_2}$ by its experimentally measured value of 4.2eV [37, 15, 42]. At each $\mathbf{p_{O_2}}$ level, oxygen chemical potential is uniquely determined according to Equation 4 and formation energies can therefore be determined. Solving for chemical potential of electron at each $\mathbf{p_{O_2}}$ level, concentrations of defects can be calculated and Kröger–Vink diagram constructed. Graphical representation of the algorithm to solve for the Fermi energy in order to construct the diagram is presented in Figure.

Resulting Kröger-Vink diagram is constructed for pure $\mathbf{ZrO_2}$,Nb containing $\mathbf{ZrO_2}$using DFT framework without correction for electron self-interaction, and Nb containing $\mathbf{ZrO_2}$ with GGA+U calculated energies. The pure $\mathbf{ZrO_2}$ is first benchmarked with our previous work done on pure $\mathbf{ZrO_2}$ [37] by making the formation energies of Nb defects artificially high. The resulting diagrams are presented in Figure 17. In the case of Nb containing $\mathbf{t - ZrO_2}$, $\mathbf{Nb_{Zr}}$ appears in significant concentration in the high $\mathbf{p_{O_2}}$ range. +1 charged $\mathbf{Nb_{Zr}}$ constitutes all of Nb defects suggesting that the dominant charge state for Nb is +5 which is the valence number of Nb atom. Our results indicate Nb+3 and Nb+4 charge states exist in negligible concentration. This result contradicts experimental study by Froideval et al [5]conducted on Nb doped zirconium alloy which reported that Nb charge state +5 was not detected at all in the formed oxide layer. Our work is consistent with Hobbs and colleagues [31]Nb+5 charge state consuming doubly charged oxygen vacancies leading to reduced oxygen diffusivity. However, Nb +2 state was not found to have significant role in contrast to their work. Positive charge introduced to the system by creation of $\mathbf{Nb_{Zr}}^{\cdot}$ is compensated by increase in electron and $\mathbf{V_{Zr}}^{''''}$ concentration and drop in $\mathbf{V_O}^{\cdot\cdot}$ in high $\mathbf{p_{O_2}}$ range of the

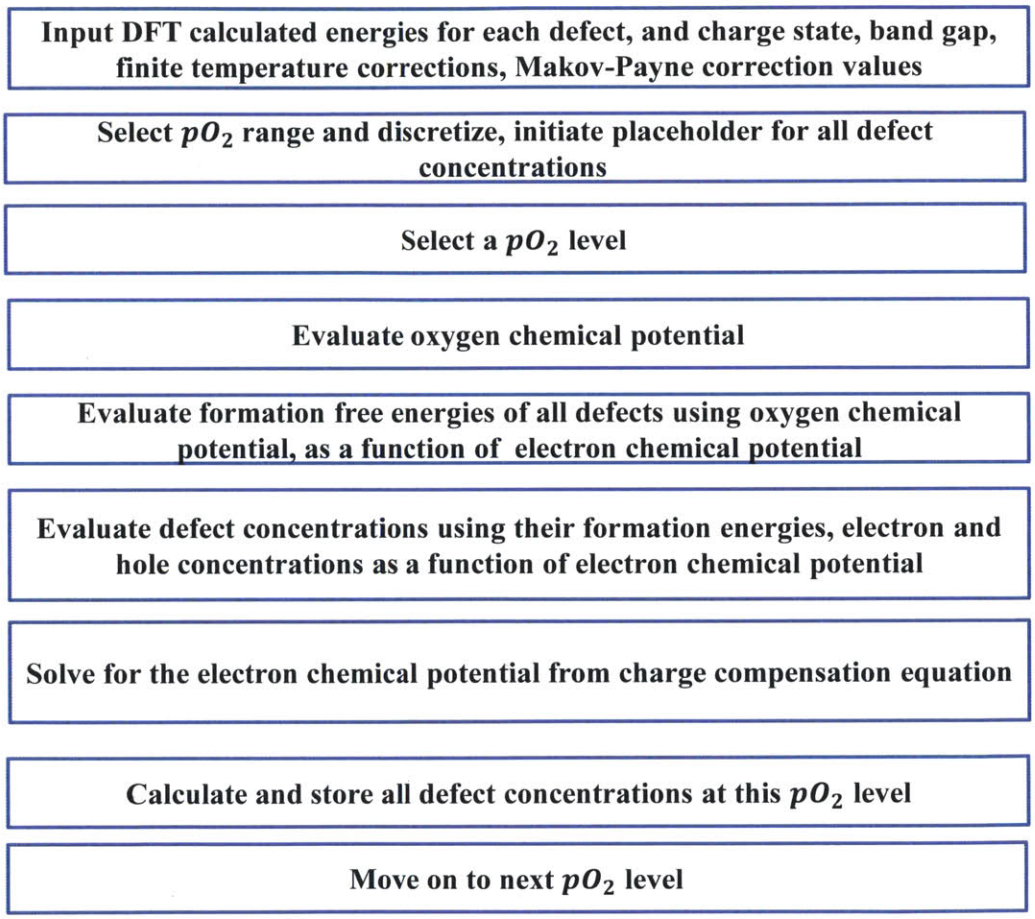

Figure 16: Schematic of the algorithm used to construct the Kroger-Vink diagram

diagram. Our current work suggest potential critical role played by charged Zr vacancy in charge compensation mechanism. The difference between pure $\mathbf{ZrO_2}$ and the Nb containing $\mathbf{ZrO_2}$ is negligible in low $\mathbf{p_{O_2}}$ range suggesting that Nb plays limited role in defect equilibrium in oxygen poor medium such as at the metal-oxide interface with $\mathbf{pO_2 \approx 10^{-20} atm}$.. Preuss et al conducts chemical analysis on corroded $\mathbf{ZIRLO^{TM}}$ in terms of segregation of alloying elements, and Nb content is found to lower in $\mathbf{ZrO_2}$ layer near alloy/oxide interface than the alloy and sub-oxide layer[32]. Our result agrees with this observation, and suggests that tetragonal $\mathbf{ZrO_2}$ formed in proximity to alloy/oxide interface might be responsible for the drop in Nb content.

Kröger–Vink diagram constructed using GGA+U calculated energy values are presented in Figure 17C. The concentration of Nb related defects were found to be lower than DFT calculated results, and the elevation in electron density occurs at higher $\mathbf{p_{O_2}}$. Similarly, the drop in concentration of doubly charged oxygen vacancy also occurs at higher $\mathbf{p_{O_2}}$ than DFT calculated result. The increased concentration of conduction band electrons at high $\mathbf{p_{O_2}}$ raises the concentration of available electrons to increase the electron conduction rate through the oxide layer. Measured electric potential for metal is always negative that suggests electron conduction may be the rate limiting[10]. On the other hand, dramatic drop in oxygen vacancy concentration acts to limit the availability of one of the species that participate in oxygen diffusion. According to Wagnerian classic oxidation theory, oxygen diffusion is the rate limiting [41, 31]. It is hard to conclude the effect of Nb defects on corrosion of Zr alloys as Nb defect has competing effects on oxygen diffusion and electron conduction, and to our knowledge there is no conclusive evidence that one process or the other is rate limiting.

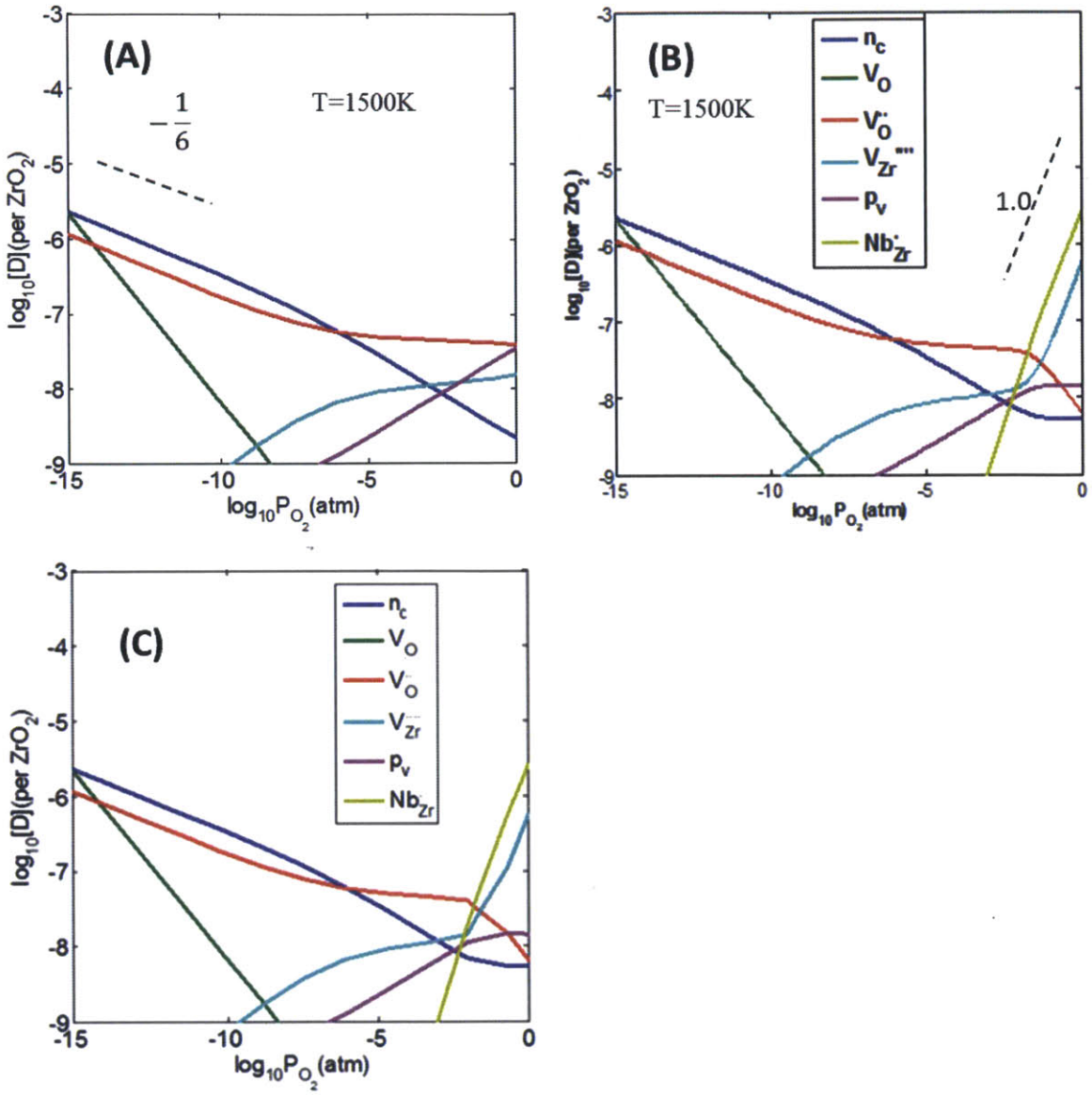

Figure 17: Kröger-Vink diagrams constructed using the results of DFT calculated values in (A) pure t-Zirconia (B) Nb containing t-Zirconia and (C) DFT+U (U=1.5eV) calculated results in Nb containing case

The temperature is too high compared to the normal reactor operating temperature, but in absence of compressive stress to stabilize tetragonal phase, it would be unrealistic to simulate it at lower temperature as tetragonal phase would not exist there.

3.2 Explaining linear regions in Kröger-Vink diagram by Mass-action law

Mass action law can be applied in conjunction with charge neutrality condition in the lattice in order to explain the linear behavior exhibited in high and low pO2 regions of Kroger-Vink diagram. Applying this simple principle to explain the result of a complex formulation such as Kroger-Vink provides an efficient way of ensuring results have realistic connections to experiment. Low pO2 region is dominated by native defects as shown by the convergence of pure $\mathbf{ZrO_2}$ case to doped $\mathbf{ZrO_2}$ there as shown in Figure 17. Mostafa et al [37]explains the linear behavior of oxygen vacancy and electronic concentration starting from charge and mass balance:

$$[\mathbf{e}] = [\mathbf{V}^{\cdot\cdot}] \tag{25}$$

$$\mathbf{O_O} = \mathbf{V_{\ddot{O}}} + \mathbf{2e} + \mathbf{O} = \mathbf{V_{\ddot{O}}} + \mathbf{2e} + \frac{\mathbf{1}}{\mathbf{2}}\mathbf{O_2(gas)} \tag{26}$$

We can then apply the mass action law using the reaction coefficient

$$\mathbf{k} = \frac{[\mathbf{e}]^{\mathbf{2}}[\mathbf{V_{\ddot{O}}}][\mathbf{pO_2}]^{\frac{\mathbf{1}}{\mathbf{2}}}}{[\mathbf{O_o}]} \tag{27}$$

we assume that host oxygen atom concentration remains unchanged, and by using equation 25

$$[\mathbf{V_{\ddot{O}}}] \sim [\mathbf{pO_2}]^{\frac{\mathbf{1}}{\mathbf{6}}} \tag{28}$$

slope of $-\frac{\mathbf{1}}{\mathbf{6}}$ can be seen on the diagram in Figure 17 showing that the linear trend can be explained by simple principles[37].

In case of dopants, charge compensation for the defect created by Niobium in the lattice

is by creation of Zirconium vacancies as demonstrated in this work. The equation for the charge and mass balance, in case of Nb doped $\mathbf{ZrO_2}$ in high pO2 range is

$$[\mathbf{Nb_{Zr}^{\cdot}}] = 4[\mathbf{V_{Zr}^{''''}}] \tag{29}$$

$$\mathbf{5Zr_{Zr} + 4Nb^{metal} + 5O_2 = 4Nb_{Zr}^{\cdot} + V_{Zr}^{''''} + 5ZrO_2} \tag{30}$$

Following the same framework as in the previous derivation, and assuming host Zirconium and Niobium metal concentrations remain unchanged,

$$[\mathbf{Nb_{Zr}^{\cdot}}] \sim [\mathbf{pO_2}] \tag{31}$$

which can also be confirmed by examining Kroger-Vink diagram in the high $\mathbf{pO_2}$ limit. We have applied mass action law with charge compensation to show that Kroger-Vink diagram converges to the result produced by this simple law in low and high $\mathbf{pO_2}$ limits.

3.3 Calculation of off-stoichometry

We have also calculated off stoichometry associated with defects in tetragonal zirconia. We define the off-stoichometry x in $\mathbf{ZrO_{2+x}}$as

$$x = \frac{2+a}{1+\delta} - 2 \tag{32}$$

with $\mathbf{a} = \sum_{\mathbf{q}}[\mathbf{O_i^q}] - \sum_{\mathbf{q}}[\mathbf{V_O^q}]$ and $\delta = \sum_{\mathbf{q}}[\mathbf{Zr_i^q}] - \sum_{\mathbf{q}}[\mathbf{V_{Zr}^q}] - \sum_{\mathbf{q}}[\mathbf{Nb_{Zr}^q}]$. The resulting off-stoichometry is given in Figure 18.

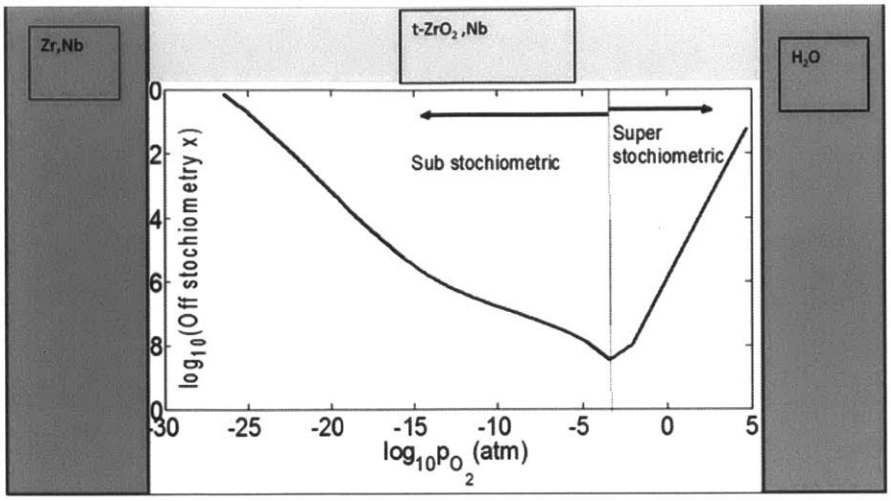

Figure 18: Stoichiometry of $\mathbf{ZrO_2}$ in the oxide layer. Gradient in the stoichiometry is associated with defect concentrations. High $\mathbf{pO_2}$ range corresponds to super stoichiometric oxide close to the oxygen rich,oxide/water interface

4 Surface oxygen exchange model

Corrosion rate in Zr containing alloys is determined by several processes including dissociative water adsorption at the oxide/water interface, oxygen diffusion and electron conduction through the oxide layer film[40, 35]. Using the results from this work, we have quantitatively assessed the impact of Nb on the surface oxygen exchange rate following an experimental finding by Jung and Tuller [46]. The results of their work suggest almost one to one correlation between the surface exchange activation energy $\mathbf{E_a}$ and the difference between conduction band minimum and chemical potential of electron as shown in Figure 19. This result suggests that electron transfer to adsorbed species is the rate limiting process for surface oxygen exchange. Under the assumption that their result can also be applied to zirconia/water interface, we apply this framework to our system.

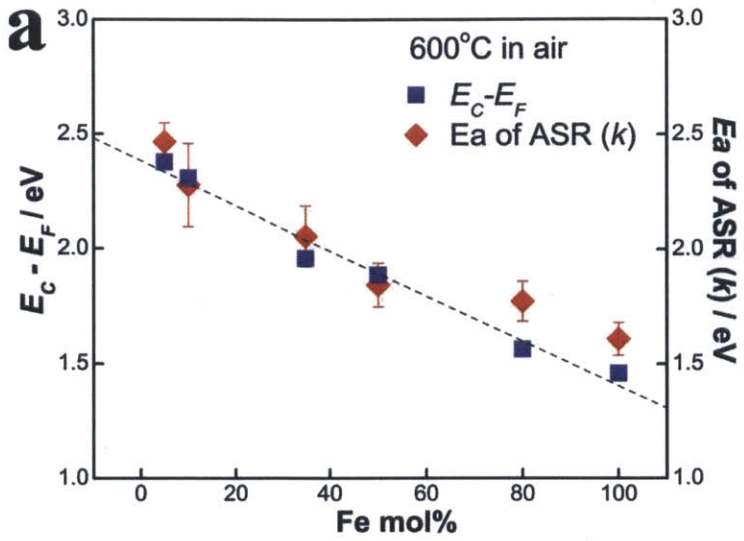

Figure 19: Correlation between activation energy $\mathbf{E_a}$ and $\mathbf{E_{CBM} - E_F}$

Activation energy of surface oxygen exchange can be approximated by the $\mathbf{E_{CBM} - E_f}$ term as in Equation 33.

$$\mathbf{k \sim e^{-\frac{E_a}{kT}} \approx e^{-\frac{(E_c - E_f)}{kT}}} \tag{33}$$

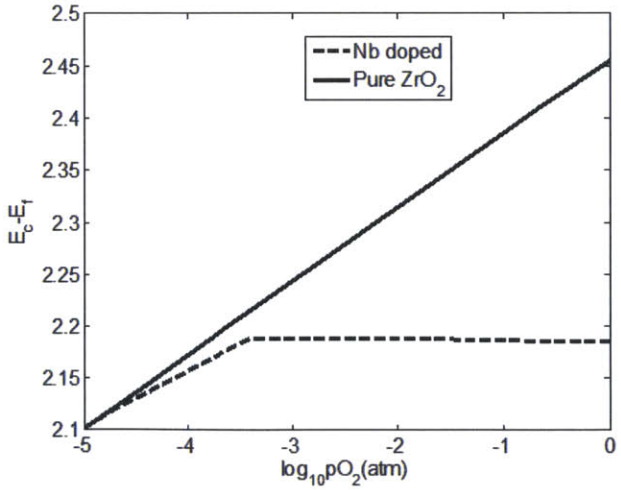

Figure 20: Difference between conduction band minimum and chemical potential of electrons for pure and Nb containing $\mathbf{ZrO_2}$ for calculating surface oxygen exchange rate

Where k is the oxygen exchange rate on oxide surface, and $\mathbf{E_a}$ is the activation energy.

Figure 20 compares pure and Nb containing $\mathbf{ZrO_2}$. The difference between conduction band minimum and chemical potential of electrons which is the activation energy in Jung and Tuller's model appears to be lowered in case of Nb containing $\mathbf{ZrO_2}$ suggesting increased rate of oxygen incorporation on the surface thus higher corrosion rate.

The result is less pronounced if we apply DFT + U framework, and the change in surface exchange rate due to Nb presence is negligibly small as in Figure 21.

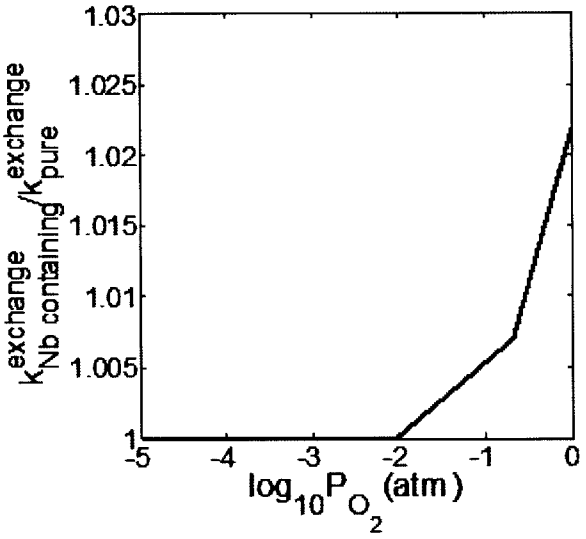

Figure 21: Change in surface exchange rate as a function of $\mathbf{pO_2}$

Jung and Tuller's model is best suited for systems where surface exchange is a rate limiting process which may be the case in latter stages of corrosion of Zr based alloys, and electron transfer is needed for reduction at the surface. For corrosion in oxygen gas, as was the case in the experiment that was conducted at the Yildiz lab at MIT[47], electron transfer was needed, and this model would be suitable. In case of corrosion in water, electron transfer may or may not be needed [38]. Regardless, the finding by Jung and Tuller has broader implication on corrosion, catalysis, and fuel cell systems as it provides powerful means of determining surface activation energy from chemical potential of electrons and vice versa.

5 Effect of applied external strain on defect energetics, and stress

Compressive stress of up to 5GPa can form at the metal/oxide interface of corroded Zr alloy as indicated in Section 1. The compressive stress is important in stabilizing tetragonal phase at relatively low temperatures at which nuclear reactors operate. Therefore, studying the effect of stress on defect energetics is important in understanding the defect formation and equilibrium in compressively strained oxides.

We evaluate the effect of compressive stress on defect formation by applying different compressive strains on computational supercell. The reason for choosing to control the strain that the strain remains constant in all types of defected cells representing oxide lattice near metal/oxide interface.

We first applied planar strain in 110 plane to undefected t-$\mathbf{ZrO_2}$ cell and relaxed in 001 (c) direction. A Defect is then created in a pre-relaxed, strained simulation cell, and allowed ionic relaxation at fixed volume. Resulting formation energies with formation energy at 0 strain set to 0 is presented in Figures 22.

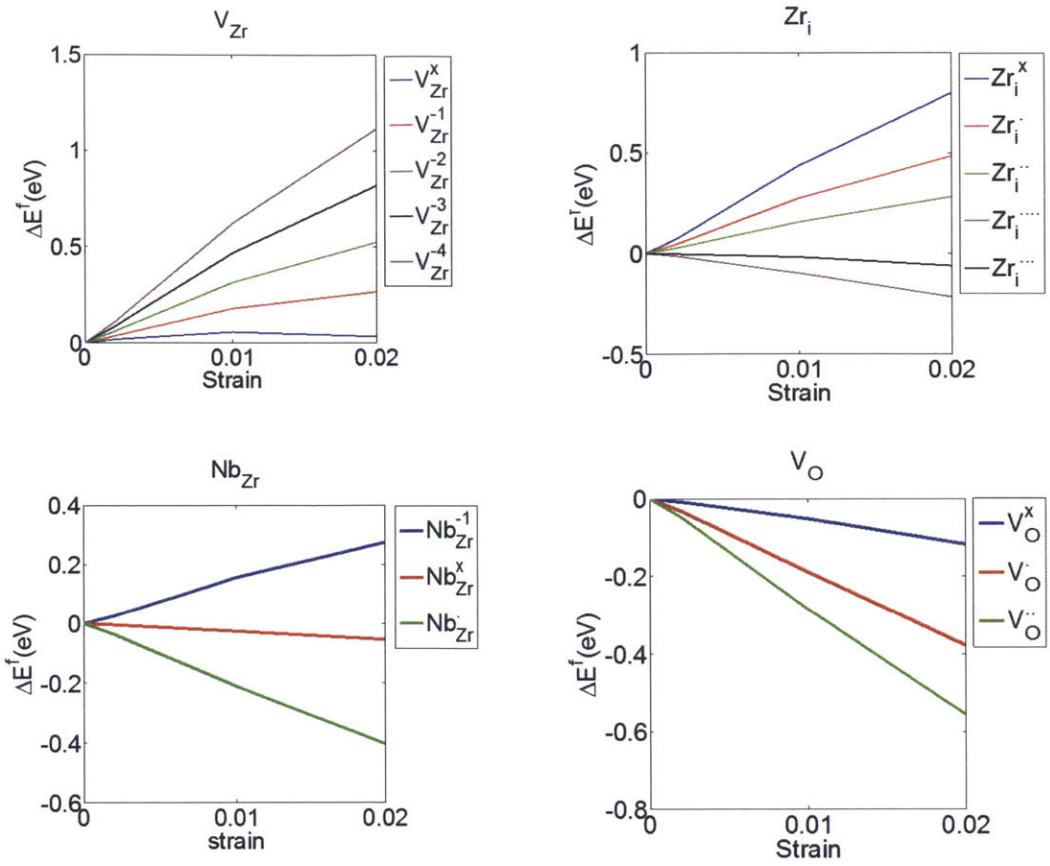

Figure 22: Formation energies as a function of strain

We summarize the observations on defect formation energy as function of compressive strain level.

1) The more positively charged the defect, the formation energy increases less as compressive strain is applied. This trend is observed throughout all defects that were considered.

2) Doubly charged oxygen vacancy which was shown to have significant contribution to the charge compensation mechanism. As compressive strain is applied, formation energy of this defect is lowered and we expect to see increase in concentration compared to zero strain/stress case.

3) The formation energy of Nb substitutional point defect corresponding to Nb+5 charge state is lowered as compressive strain is applied. As $\mathbf{Nb_{Zr}^{\cdot}}$ is shown to participate in charge compensation with high concentration, and we expect elevated concentration as compressive

strain is present.

4) Quadruply charged Zirconium vacancy is found to be the main compensation to positive charge introduced by $\mathbf{Nb_{Zr}}$. As compressive strain is applied, formation energy is increased by about 1.2 eV leading to lower concentration in equilibrium.

5) Doubly charged oxygen vacancy, an important contributor of positive charge to the formed oxide is shown to have lower formation energy when compressive strain is applied, and this will contribute to it's elevated concentration in equilibrium.

We also examined the addition stress introduced by a defect. We define the additional stress as in Equation 34.

$$\Delta\sigma_x^{added} = \sigma_x^{defected} - \sigma_x^{undefected} \tag{34}$$

The DFT calculated additional stress for different defects is given in Figure 23. The reason for choosing to plot σ_x is that the strain we applied is symmetric with x and y direction, and the cell is relaxed in the z direction.

Generally in all defects and charge states, applied compressive strain either decreases (by relaxing the computational cell) or does not alter the additional stress introduced by a defect. In cases of $\mathbf{Nb_{Zr}}$, $\mathbf{V_{Zr}}$, $\mathbf{V_O}$ point defects, applied external compressive strain was shown to relax the stress introduced by a point defect.

Figure 24 shows the formation energies of important defects as a function of electron chemical potential at different strain values. Dominant charge states of these defects over accessible Fermi levels are not significantly affected by applied compressive strain.

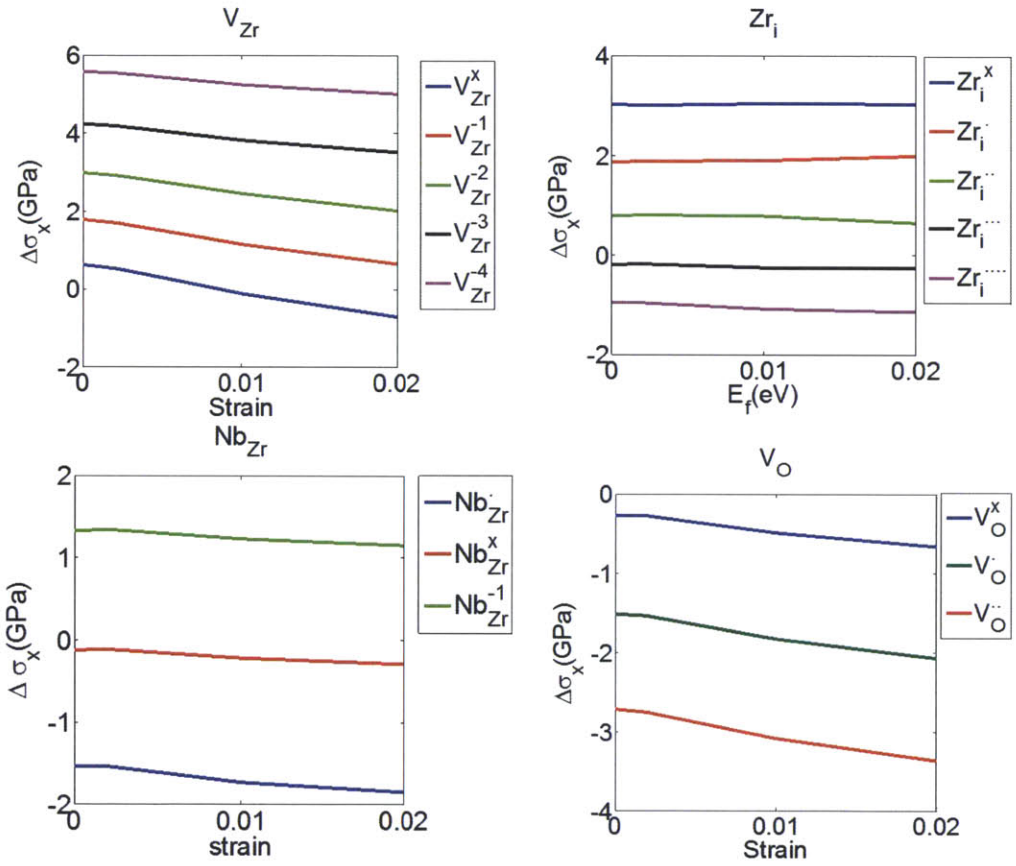

Figure 23: Additional stress due to defect as a function of strain

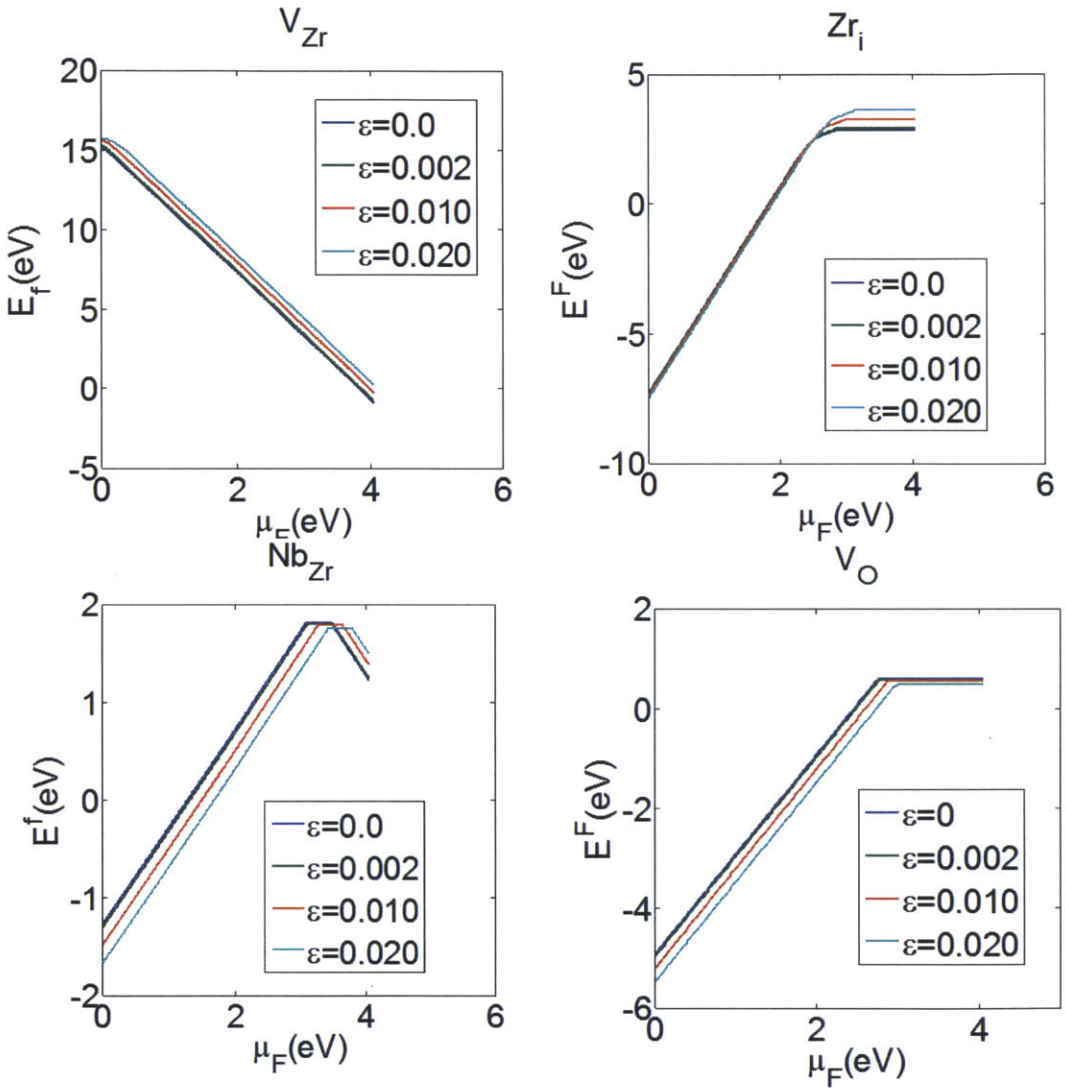

Figure 24: The formation energies of important defects as a function of chemical potential of electrons at different strain values

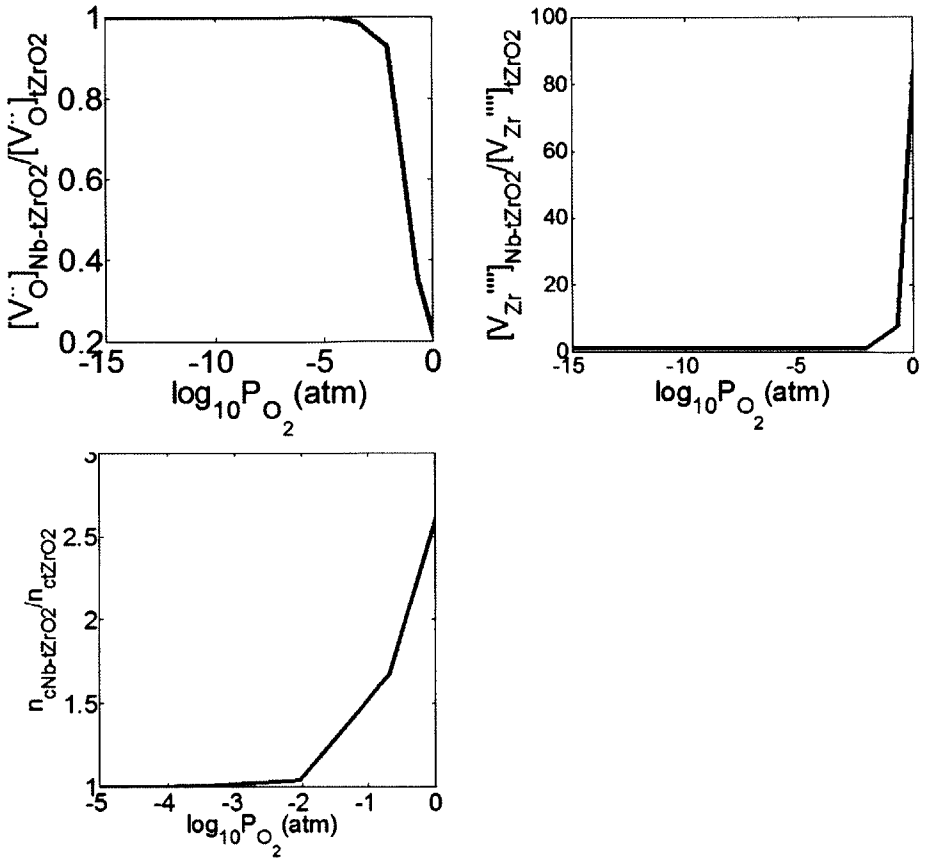

Figure 25: Ratio of (A) doubly charged oxygen vacancies,(B) quadruply charged Zirconium vacancy in Nb containing and pure $\mathbf{t-ZrO_2}$.

6 Implications on corrosion kinetics

From the experimental literature, oxygen bulk diffusion, bulk ionic transport, and electron transport through the formed oxide layer are known to be important in determining the corrosion rate of Zr based alloys [35]. Our simulation suggests reduced oxygen diffusion rate in case of Nb containing oxide as the concentration of doubly charged oxygen vacancy drops significantly as in Figure 25 since oxygen diffusion coefficient can be defined as in Equation 35.

$$\mathbf{D_{self} = D_v[V_{\ddot{O}}]} \tag{35}$$

The concentration of zirconium vacancy which is precursor to Zr diffusion to the water interface is elevated as a result of Nb point defects as shown in Figure 25 suggesting enhanced ionic transport to facilitate the corrosion process. Mobility values of Zr+4 and O-2 species in zirconia as reported in the literature are $\mathbf{D_v^{Zr} = 10^{-20} m^2 s^{-1}}$ and $\mathbf{D_v^{O} = 10^{-12} m^2 s^{-1}}$ respectively [11]. The dominant impact will therefore come from decrease in oxygen diffusion rate which is mediated by oxygen vacancy resulting in reduced corrosion rate for Nb containing alloys. Lastly, a slight increase in conduction band electrons due to the added Nb exhibited in high pO2 range which corresponds to oxide/water interface shown in Figure 4 acts to elevate the number of available electrons participating in charge transfer through oxide layer assisting corrosion.

7 Conclusion

In this work, the effect of alloying Niobium on defect concentration in tetragonal phase of zirconia is evaluated. We calculated the formation energies of certain point defects that mediate transport processes critical for corrosion, and Kröger -Vink diagram is constructed with and without Nb defects present in order to see the effect of Nb on equilibrium defect concentrations. Our result at high temperature with no strain effect indicates that Niobium enhances zirconium transport through the oxide layer and electron transfer on the surface while slowing down oxygen diffusion from surface to the metal/oxide interface. The higher mobility oxygen diffusion rate means effect of Nb comes predominantly from oxygen diffusion which is mediated by oxygen vacancy implying reduced corrosion rate. As part of the effort to characterize the nature of Nb defect, we examined the charge state of Nb in t-ZrO2 as there is controversy in the literature. Niobium is found to be stable in Nb+3, Nb+4,Nb+5 charge states while Nb+5 exists in highest concentration in calculation without strain effect included. When the effect of applied external compressive strain on energetics and stress of different types of defects, and formation energy is quantified as a function of strain. It is observed that the more positively charged the defect, the formation energy increases less as compressive strain is applied. Experimental observation of Nb segregation to the surface observed in a parallel work in our group was found to be consistent with the predicted higher concentration of Nb substitutional defect and higher Zirconium vacancy concentration. In future, the defect equilibrium concentrations should be re-calculated including strain effects at lower temperature in order to simulate a more realistic reactor operating condition. We believe DFT can be applied to better understand the effect of alloy constituents on corrosion on atomistic level providing means to develop alloys with improved corrosion resistance.

References

[1] Thermochemical tables.

[2] D.Gavillet D.Grolimund C.Borca J.Krbanjevic C.Degueldre A. Froideval, S.Abolhassani. Microprobe analysis of neutron irradiated and autoclaved Zirconium Niobium claddings using synchrotron-based hard X-ray imaging and spectroscopy. *Journal of nuclear materials*, 285:346–350, 2008.

[3] M. Blat-Yrieix L. Legras P. Frankel M. Preuss C. Curfs G. Parry A. Ly, A. Ambard and Y. Brechet. Understanding Crack Formation at the Metal/Oxide Interface During Corrosion of Zircaloy-4 Using a Simple Mechanical Model. *Journal of ASTM International*, 8(9):1, 2011.

[4] I.Tanaka A. Togo, F.Oba. First-principles calculations of the ferroelastic transition between rutile-type and CaCl2-type SiO2 at high pressures. *PHYSICAL REVIEW B*, 78:134106, 2008.

[5] C.U.Segre M.A.Pouchon D.Grolimund A.Froideval, C.Degueldre. Niobium speciation at the metal/oxide interface of corroded niobium-doped Zircaloys: A X-ray absorption near-edge structure study. *Corrosion Science*, 50:1313 1320, 2008.

[6] A.Motta. Waterside Corrosion in Zirconium Alloys. *Advanced Fuel Performance: Modeling and Simulation Research Summary*, 63:59–63, 2011.

[7] N. Aschcroft and N. Mermin. *Solid State Physics*. Brooks/Cole, 1976.

[8] A.Motta H.G.Kim Y.H.Jeong J.Y.Park-R.Comstock B.Lai Z.Cai A.Yilmazbayhan, M.G.Silva. CHARACTERIZATION OF OXIDES FORMED ON MODEL Zirconium ALLOYS IN 360° C WATER USING MICRO-BEAM SYNCHROTRON RADIATION. In *Proceedings of the 12th International Conference on Environmental Degradation of Materials in Nuclear Power System -Water Reactors*, 2005.

[9] A.T. Motta R.J.Comstock A.Yilmazbayhan, E.Breval. Transmission electron microscopy examination of oxide layers formed on Zr alloys. *Journal of nuclear materials*, 349:265–281, 2006.

[10] B.Cox. Some thoughts on the mechanism of in-reactor corrosion in zirconium alloys. *JOURNAL OF NUCLEAR MATERIALS*, 336:331–368, 2005.

[11] G. Bart C.Degueldre, A.Amato. Muon Spin Relaxation Measurements on Zirconia Samples. *Scripta Materialia*, 54:1211–1216, 2005.

[12] J.Neugebauer C.G.Van deWalle. First-principles calculations for defects and impurities: Applications to III-nitrides. *JOURNAL OF APPLIED PHYSICS*, 95(8):3851–3879, 2004.

[13] J.A.Steckel David S. Sholl. *Density Functional Theory: A Practical Introduction.* John Wiley & Sons, 2009.

[14] G.Kresse D.Joubert. From ultrasoft pseudopotentials to the projector augmented-wave method. *PHYSICAL REVIEW B*, 59(3):1758, 1999.

[15] D.W.McComb. Bonding and electronic structure in zirconia pseudopolymorphs investigated by electron energy-loss spectroscopy. *PHYSICAL REVIEW B*, 54:04233–6, 1996.

[16] R.Smith G.Henkelman E.Sanville, S.D.Kenny. An improved grid-based algorithm for Bader charge allocation. *Journal of Computational Chemistry*, 28:899, 2007.

[17] A.Jain C.J. Moore G.Ceder G.Hautier, S.P.Ong. Accuracy of density functional theory in predicting formation energies of ternary oxides from binary oxides and its implication on phase stability. *PHYSICAL REVIEW B*, 85:155208, 2012.

[18] H.Jónsson G.Henkelman, A.Arnaldsson. A fast and robust algorithm for Bader decomposition of charge density. *Computational Materials Science*, 36:254, 2006.

[19] M.C.Payne G.Makov. Periodic boundary conditions in ab initio calculations. *PHYSICAL REVIEW B*, 51(7):2014, 1995.

[20] R.J.Comstock H. H.Shah D.J.Colburn-M.Dahlback L.Hallstadius H.K.Yueh, R.L.Kesterson. Improved ZIRLO Cladding Performance through Chemistry and Process Modifications. *Journal of ASTM International*, 2:1–10, 2005.

[21] P.Li I.W.Chen. Effect of Dopants on Zirconia Stabilization-An X-ray Absorption Study: iii, Charge-Compensating Dopants. *Journal of American Ceramics society*, 77(5):1289–1295, 1994.

[22] A.V.Virkar D.R.Clarke J.Chevalier, L.Gremillard. The Tetragonal-Monoclinic Transformation in Zirconia: Lessons Learned and Future Trends. *Journal of the American Ceramic Society*, 92:1901–1920, 2009.

[23] G. Kresse J.Furthmüller. Efficiency of ab-initio total energy calculations for metals and semiconductors using a plane-wave basis set. *Computational Materials Science*, 6:15, 1996.

[24] G.Kresse J.Furthmüller. Efficient iterative schemes for ab initio total-energy calculations using a plane-wave basis set. *PHYSICAL REVIEW B*, 54:11169, 1996.

[25] G.Kresse J.Hafner. Ab initio molecular dynamics for liquid metals. *PHYSICAL REVIEW B*, 47(1):558, 1993.

[26] G.Kresse J.Hafner. Ab initio molecular-dynamics simulation of the liquid-metal-amorphous-semiconductor transition in germanium. *PHYSICAL REVIEW B*, 49(1):14251, 1994.

[27] A.Chartier J.P.Crocombette, D.Torumba. Charge states of point defects in uranium oxide calculated with a local hybrid functional for correlated electrons. *PHYSICAL REVIEW B*, 83:184107, 2011.

[28] M.Ernzerhof J.P.Perdew, K.Burke. Generalized gradient approximation made simple. *PHYSICAL REVIEW LETTER*, 77:3865, 1996.

[29] M.Ernzerhof J.P.Perdew, K.Burke. Erratum: Generalized gradient approximation made simple. *PHYSICAL REVIEW LETTER*, 78:1396, 1997.

[30] L.G.Liu. New High Pressure Phases of ZrO2 and HfO2. *Journal of Physical Chemistry of Solids*, 41:331–334, 1980.

[31] S.P.Mangin M.Treska G.Hunter L.W.Hobbs, V.B.Rosen. Oxidation Microstructures and Interfaces in the Oxidized Zirconium Knee. *Applied Ceramic Technology*, 2(3):221, 2005.

[32] D.Hudson E.Polatidis-N. Ni J.Wei C.English S.Storer K. B.Chong M.Fitzpatrick P.Wang J.Smith C.Grovenor G.Smith J.Sykes B.Cottis S.Lyon L.Hallstadius B.Comstock A.Ambard M.Blat-Yrieix M. Preuss, S.Lozano-Perez. Studies Regarding Corrosion Mechanisms in Zirconium Alloys. *Journal of ASTM International*, 8(9), 2010.

[33] N.Ver M.Große, M.Steinbruck. Oxidation of Advanced Zirconium Cladding Alloys in Steam at Temperatures in the Range of 600-1200C. *Oxidation metal*, 76(76):215–232, 2010.

[34] D.R.Bates M.S.Khan, M.S.Islam. Cation doping and oxygen diffusion in zirconia: a combined atomistic simulation and molecular dynamics study. *Journal of Materials chemistry*, 8(10):2299–2307, 1998.

[35] A.Jokisaari-K.Thornton M.Youssef, B.Yildiz. Waterside Corrosion of Zircaloy-4: Underlying Phenomena, Current Models and Planned Physics-Based Models.

[36] B.Yildiz M.Youssef. Hydrogen Defects in Tetragonal ZrO2.

[37] B.Yildiz M.Youssef. Intrinsic point-defect equilibria in tetragonal ZrO2: Density functional theory analysis with finite-temperature effects. *PHYSICAL REVIEW B*, 86:144109, 2012.

[38] J.C.Garcia N.A.Deskins. Detailing Ionosorption over TiO2, ZrO2, and HfO2 from First Principles. *Journal of Physical Chemistry C*, 116:16573–16581, 2012.

[39] C.Lemaignan C.Valot M.Lallemant N.Petigny, P.Barberis. In situ XRD analysis of the oxide layers formed by oxidation at 743 K on Zircaloy 4 and Zr-1NbO. *Journal of nuclear materials*, 280:318 330, 2000.

[40] N.Ramasubramanian J.Peybernes D.Pecheur P.Billot, S.Yagnik. The Role of Lithium and Boron on the Corrosion of Zircaloy-4 Under Demanding PWR-Type Conditions. *Zirconium in the nuclear Industry: 13th International Symposium ASTM STP*, 1423:169–189, 2002.

[41] P.Kofstad. *High Temperature Corrosion.* Elsevier Applied Science, 1988.

[42] F.S.Ohuchi Y.N.Xu W.Y.Ching R.H.French, S.J.Glass. Experimental and theoretical determination of electronic structure and optical properties of three phases of ZrO2. *PHYSICAL REVIEW B*, 49:5133 5142, 1994.

[43] S.Watanabe S. Kasamatsu, T.Tada. Theoretical analysis of space charge layer formation at metal/ionic conductor interfaces. *Solid State Ionics*, 183:20, 2011.

[44] S.Y.Savrasor C. J. Humphreys-A.P.Sutton S.L.Dudarev, G.A.Botton. Electron-energy-loss spectra and the structural stability of nickel oxide: An LSDA1U study. *PHYSICAL REVIEW B*, 57:1505–1509, 1998.

[45] G. Henkelman W. Tang, E. Sanville. A grid-based Bader analysis algorithm without lattice bias. *Journal of Physics: Condensed Matter*, 21:084204, 2009.

[46] H.L.Tuller W.Jung. A New Model Describing Solid Oxide Fuel Cell Cathode Kinetics. *Advanced Energy Materials*, 1:1184–1191, 2011.

[47] B.Yildiz W.Ma. (in preparation).

[48] P.Bossis M.Pijolat Y. Dali, M.Tupin. EFFECT OF ALLOYING ELEMENTS ON THE OXIDATION KINETICS OF ZIRCONIUM BASED ALLOYS UNDER HIGH PRESSURE STEAM. *NACE international*, -:07601, 2007.

[49] J.N.Jang Y.S.Kim, Y.H.Jeong. Stress Measurements During Thin Film Zirconium Oxide Growth. *Journal of nuclear materials*, 412:217–220, 2011.

8 Appendix A

Kroger-Vink notation

Notation	Chemical species
$\mathbf{V_O^x}$	Neutral oxygen vacancy
$\mathbf{V_O^{\cdot}}$	+1 charged oxygen vacancy
$\mathbf{V_O^{'}}$	+1 charged oxygen vacancy
$\mathbf{V_{Zr}^x}$	Neutral zirconium vacancy
$\mathbf{Nb_{Zr}^x}$	Neutral Niobium atom on Zirconium site
$\mathbf{Zr_i^x}$	Neutral Zirconium interstitial
$(\mathbf{Nb_{Zr}} - \mathbf{V_O})^x$	Defect complex of oxygen vacancy bound to $\mathbf{Nb_{Zr}}$(total charge 0)

Table 10: Kroger-Vink notation

9 Appendix B

MATLAB script converted from FORTRAN to include Niobium defects and finite temperature effects.

```
%phonons included
%electrons calculated using integral formula
%experimental band gap used.
%DFT+U,J=1.5 is used for Nb_Zr defects
Ef=1; Ce=1; Ch=1; COV=1; COV1=1; COV2=1; COI=1; COI_1=1; COI_2=1;
CZV_4=1; CZV_3=1; CZV_2=1; CZV_1=1; CZV=1; CZI=1; CZI1=1; CZI2=1;
CZI3=1; CZI4=1; CNbI=1; CNbI1=1; CNbI2=1; CNbI3=1; CNbI4=1; CNbI5=1;
CNbOV1NNn2=1; CNbOV1NNn1=1; CNbOV1NN0=1; CNbOV1NN1=1;
CNbOV1NN2=1; CNbOV1NN3=1;
CNb_sub_n1=1; CNb_sub_0=1; CNb_sub_1=1;
prec=1.0E-4; n=100; kB=8.6173324E-5; Vfu=35.2016E-30;

%!The volume per formula unit in m3

h=6.626068E-34;pi=3.14159265;me=9.10938188E-31;
Eox=-1.0; Eox=0; T=1500.000000; %temperature
muo_0=0.5*(0.096775438-.98542082E+01)-3.50125847/2;
E_shift=0.3; beta=1.0/(T*kB);
%COMPUTE THE HOLE AND ELECTRON PREFACTOR
Ne=2*pi*me*T*1.3806503e-23;
Ne=Ne/(h^2); Ne=Ne*sqrt(Ne); Ne=Ne*2.0*Vfu;

%changed from per unit volume to per chemical formula

Nh=Ne; muo_max=muo_0+10.0;
% !PO2=1E2
muo_min=muo_0-10.0; %!PO2=10E-50 step=(muo_max-muo_min)/(n-1);
muo=zeros(1,n); logPO2=zeros(1,n); Ef=zeros(1,n); Ce=zeros(1,n);
Ch=zeros(1,n); COV=zeros(1,n); COV1=zeros(1,n); COV2=zeros(1,n);
COI=zeros(1,n); COI_1=zeros(1,n); COI_2=zeros(1,n); CZV_4=zeros(1,n);
CZV_3=zeros(1,n); CZV_2=zeros(1,n); CZV_1=zeros(1,n); CZV=zeros(1,n);
CZI=zeros(1,n); CZI1=zeros(1,n); CZI2=zeros(1,n);

CZI3=zeros(1,n); CZI4=zeros(1,n);
```

```
CNb_sub_n1=zeros(1,n); CNb_sub_0=zeros(1,n); CNb_sub_1=zeros(1,n);
CNbI=zeros(1,n); CNbI1=zeros(1,n); CNbI2=zeros(1,n); CNbI3=zeros(1,n);
CNbI4=zeros(1,n); CNbI5=zeros(1,n);CNbOV1NNn2=zeros(1,n);
CNbOV1NNn1=zeros(1,n); CNbOV1NN0=zeros(1,n); CNbOV1NN1=zeros(1,n);
CNbOV1NN2=zeros(1,n); CNbOV1NN3=zeros(1,n);
Gd1=zeros(1,n); Gd2=zeros(1,n); Gd3=zeros(1,n);
Gd4=zeros(1,n); Gd5=zeros(1,n); Gd6=zeros(1,n);
GdV_4=zeros(1,n); GdV_3=zeros(1,n); GdV_2=zeros(1,n); GdV_1=zeros(1,n);
GdV=zeros(1,n);GdI=zeros(1,n); GdI1=zeros(1,n); GdI2=zeros(1,n);
GdI3=zeros(1,n);GdI4=zeros(1,n); GdNbI=zeros(1,n); GdNbI1=zeros(1,n);
GdNbI2=zeros(1,n); GdNbI3=zeros(1,n);

GdNbI4=zeros(1,n); GdNbI5=zeros(1,n);

GdNbOV1NNn2=zeros(1,n); GdNbOV1NNn1=zeros(1,n);
GdNbOV1NN0=zeros(1,n); GdNbOV1NN1=zeros(1,n);
GdNbOV1NN2=zeros(1,n); GdNbOV1NN3=zeros(1,n);
GdNb_sub_n1=zeros(1,n); GdNb_sub_0=zeros(1,n);

GdNb_sub_1=zeros(1,n);

for k=1:n
    muo(k)=muo_min+(k-1)*step;
    logPO2(k)=muo(k)-muo_0;
    logPO2(k)=exp((2.0*logPO2(k))/(kB*T));
    logPO2(k)=log10( logPO2(k));
end;
Egap=3.8998+E_shift;%!  ; %DFT calculated
EVBM=2.871667; ECBM=2.871667+Egap+E_shift; eps=39.8;
%!  %the dielectric constant of T-ZrO2 experimental
Ep=-.90913442E+03;%!  ;%Perfect Crystal Energy
E_nb=-.14126783E+04/81-(( -3.50125847-4.04104428) / 2);
%Phonon contributions
FP=-4577.1948296*0.01;

%Perfect crystal free energy, Converted from kJ/mol to eV

FOV=(-4567.9061*0.01)-FP; FOV1=(-4541.383*0.01)-FP;
FOV2=(-4541.383*0.01)-FP; FI=(-4524.4506*0.01)-FP;
FI_1=(-4541.261*0.01)-FP; FI_2=(-4541.261*0.01)-FP;
```

```
FZV_4=(-4509.369*0.01)-FP; FZV_3=(-4625.8657427*0.01)-FP;
FZV_2=(-4583.9994239*0.01)-FP; FZV_1=(-4569.4425803*0.01)-FP;
FZV=(-4593.9327033*0.01)-FP; FZI=(-4592.825*0.01)-FP;
FZI1=(-4588.3587415*0.01)-FP; FZI2=(-4576.046*0.01)-FP;
FZI3=(-4550.2961059*0.01)-FP; FZI4=(-4509.737*0.01)-FP;
FEdNbI1= -45.990334788-FP; FEdNbI2=-45.803947531-FP;
FEdNbI3=-45.803947531-FP; FEdNbI4=-45.803947531-FP;
FEdNbI5=-45.803947531-FP; FEdNbOV1NNn1=-45.857812170-FP;
FEdNbOV1NN0=-45.718703207-FP; FEdNbOV1NN1=-45.306289795-FP;
FEdNbOV1NN2=-45.306289795-FP; FEdNbOV1NN3=-44.951612036-FP;
FEdNb_sub_n1=-46.270719828-FP; FEdNb_sub_0=-45.297104597-FP;
% FEdNb_sub_1=-44.742515593-FP;
%Oxygen VACACNY
Ed1=-.89859010E+03-Ep+FOV;
Ed2=-0.904525479133E+03-Ep+(1.962787/eps)+FOV1+8.0;
Ed3=-0.910595931987E+03-Ep+(7.851147/eps)+FOV2;
%Oxygen Interstitial Interstitial Ed4=-0.91226904E+03-Ep+FI;
%[110] Dumbbell Ed5=-0.90764285E+03-Ep+(1.962787/eps)+FI_1+8.0;
%[110]Dumbbell Ed6=-0.90395336E+03-Ep+(7.851147/eps)+FI_2;
%Zircnoium Vacacny
EdV_4= -0.87346205E+03-(93.0/96.0)*Ep+(31.404589/eps)+FZV_4;
EdV_3=-0.87630914E+03-(93.0/96.0)*Ep+(17.665081/eps)+FZV_3;
EdV_2=-0.87911176E+03-(93.0/96.0)*Ep+(7.851147/eps)+FZV_2;
EdV_1=-0.88194619E+03-(93.0/96.0)*Ep+(1.962787/eps)+FZV_1;
EdV=-0.88489643E+03-(93.0/96.0)*Ep+FZV;
%interstitial Zirconium
EdI=-0.91480490E+03-(99.0/96.0)*Ep+FZI;
EdI1=-0.92084400E+03-(99.0/96.0)*Ep+(1.962787/eps)+FZI1;
EdI2=-0.92692901E+03-(99.0/96.0)*Ep+(7.851147/eps)+FZI2;
EdI3=-0.93255656E+03-(99.0/96.0)*Ep+(17.665081/eps)+FZI3;
EdI4=-0.93831793E+03-(99.0/96.0)*Ep+(31.404589/eps)+FZI4;
%Nb interstitial
EdNbI=-.91484891E+03-Ep-E_nb+250;
EdNbI1=-.92197205E+03+FEdNbI1-Ep-E_nb+(1.962787/eps);
EdNbI2=-.92737948E+03+FEdNbI2-Ep-E_nb+(7.851147/eps);
EdNbI3=-.93261877E+03+FEdNbI3-Ep-E_nb+(17.665081/eps);
EdNbI4=-.93792171E+03+FEdNbI4-Ep-E_nb+(31.404589/eps);
EdNbI5=-.94332151E+03+FEdNbI5-Ep-E_nb+(49.053839/eps);
```

```
%Nb substitution V_o
EdNbOV1NNn2=-.88517718E+03-Ep-E_nb+(7.851147/eps);
EdNbOV1NNn1=-.891358959227E+03+FEdNbOV1NNn1-Ep-E_nb+(1.962787/eps);
EdNbOV1NN0=-.89739678E+03+FEdNbOV1NN0-Ep-E_nb;
EdNbOV1NN1=-.90338177E+03+FEdNbOV1NN1-Ep-E_nb+(1.962787/eps);
EdNbOV1NN2=-.90905535E+03+FEdNbOV1NN2-Ep-E_nb+(7.851147/eps);
EdNbOV1NN3=-.91464150E+03+FEdNbOV1NN3-Ep-E_nb+(17.665081/eps);
%Nb substitution, DT+U,J=1.5
EdNb_sub_n1=-.90005850E+03+FEdNb_sub_n1-Ep-E_nb+(1.961871/eps);
EdNb_sub_0=-.90612945E+03+FEdNb_sub_0-Ep-E_nb;
EdNb_sub_1=-.91209725E+03+FEdNb_sub_1-Ep-E_nb+(1.972432/eps);
old_root=0;
Fermi_energies=[];
v=0; w=[];
%CHARGE NEUTRALITY, THE chemical potential of electrons IS FIXED
for k=1:n
    Efl=EVBM+prec; Efr=ECBM-prec;
    while
        no_solution=0;
        if Efr<EVBM
            old_root=0;
            no_solution=1;
            break
        end;
        %start Baracketing, Compute the formation energies on the right
        %!Oxygen VACACNY Gd1r=Ed1+muo(k);
        Gd2r=Ed2+muo(k)+Efr; Gd3r=Ed3+muo(k)+2.0*Efr;
        %!Oxygen Interstitial Interstitial
        Gd4r=Ed4-muo(k); Gd5r=Ed5-muo(k)-Efr; Gd6r=Ed6-muo(k)-2.0*Efr;
        %!Zircnoium Vacacny
        GdV_4r=EdV_4-2.0*muo(k)-4.0*Efr;
        GdV_3r=EdV_3-2.0*muo(k)-3.0*Efr;
        GdV_2r=EdV_2-2.0*muo(k)-2.0*Efr;
        GdV_1r=EdV_1-2.0*muo(k)-Efr;
        GdVr=EdV-2.0*muo(k);
        %!interstitial Zirconium
        GdIr=EdI+2.0*muo(k);
        GdI1r=EdI1+2.0*muo(k)+Efr;
```

```
GdI2r=EdI2+2.0*muo(k)+2.0*Efr;
GdI3r=EdI3+2.0*muo(k)+3.0*Efr;
GdI4r=EdI4+2.0*muo(k)+4.0*Efr;
% Nb interstitial
GdNbIr=EdNbI;
GdNbI1r=EdNbI1+1.0*Efr;
GdNbI2r=EdNbI2+2.0*Efr;
GdNbI3r=EdNbI3+3.0*Efr;
GdNbI4r=EdNbI4+4.0*Efr;
GdNbI5r=EdNbI5+5.0*Efr;
%O vacancy bound to Nb substitution
GdNbOV1NNn2r=EdNbOV1NNn2+(Ep/32-muo(k))-2.0*Efr;
GdNbOV1NNn1r=EdNbOV1NNn1+(Ep/32-muo(k))-1.0*Efr;
GdNbOV1NNOr=EdNbOV1NNO+(Ep/32-muo(k))-0.0*Efr;
GdNbOV1NN1r=EdNbOV1NN1+(Ep/32-muo(k))+1.0*Efr;
GdNbOV1NN2r=EdNbOV1NN2+(Ep/32-muo(k))+2.0*Efr;
GdNbOV1NN3r=EdNbOV1NN3+(Ep/32-muo(k))+3.0*Efr;
% Nb substitution
GdNb_sub_n1r=EdNb_sub_n1+(Ep/32-2.0*muo(k))-1.0*Efr;
GdNb_sub_0r=EdNb_sub_0+(Ep/32-2.0*muo(k));
GdNb_sub_1r=EdNb_sub_1+(Ep/32-2.0*muo(k))+1.0*Efr;
%!  To Avoid Negative Formation ENERGEIS
if Gd1r<0.0 || Gd2r<0.0 || Gd3r<0.0 || Gd4r<0.0 || Gd5r<0.0 ...
|| Gd6r<0.0 || GdV_4r<0.0 || GdV_3r<0.0 || GdV_2r<0.0...
|| GdV_1r<0.0 || GdVr<0.0 || GdI4r<0.0 || GdI3r<0.0...
|| GdI2r<0.0 || GdI1r<0.0 || GdIr<0.0 || GdNbIr<0.0...
|| GdNbI1r<0.0 || GdNbI2r<0.0 || GdNbI3r<0.0...  || GdNbI4r<0.0...||
GdNbI5r<0.0 || GdNbOV1NNn2r<0.0 || GdNbOV1NNn1r<0.0...
|| GdNbOV1NNOr<0.0 || GdNbOV1NN1r<0.0 || GdNbOV1NN2r<0.0||...
GdNbOV1NN3r<0.0 || GdNb_sub_n1r<0.0 || GdNb_sub_0r<0.0 ...
|| GdNb_sub_1r<0.0
Efr=Efr-0.0001; continue end;
if Efl>ECBM
    old_root=0;
    no_solution=1;
    break
end;
%!Compute the formation energies on the left
```

```
%!Oxygen VACACNY
Gd1l=Ed1+muo(k); Gd2l=Ed2+muo(k)+Efl; Gd3l=Ed3+muo(k)+2.0*Efl;
%!Oxygen Interstitial Interstitial
Gd4l=Ed4-muo(k); Gd5l=Ed5-muo(k)-Efl; Gd6l=Ed6-muo(k)-2.0*Efl;
%!Zircnoium Vacany
GdV_4l=EdV_4-2.0*muo(k)-4.0*Efl; GdV_3l=EdV_3-2.0*muo(k)-3.0*Efl;
GdV_2l=EdV_2-2.0*muo(k)-2.0*Efl; GdV_1l=EdV_1-2.0*muo(k)-Efl;
GdVl=EdV-2.0*muo(k);
%!Interstitial Zirconium
GdIl=EdI+2.0*muo(k); GdI1l=EdI1+2.0*muo(k)+Efl;
GdI2l=EdI2+2.0*muo(k)+2.0*Efl; GdI3l=EdI3+2.0*muo(k)+3.0*Efl;
GdI4l=EdI4+2.0*muo(k)+4.0*Efl;
%Nb interstitital
GdNbIl=EdNbI; GdNbI1l=EdNbI1+1.0*Efl;
GdNbI2l=EdNbI2+2.0*Efl; GdNbI3l=EdNbI3+3.0*Efl;
GdNbI4l=EdNbI4+4.0*Efl;GdNbI5l=EdNbI5+5.0*Efl;
%O vacancy bound to Nb substiution
GdNbOV1NNn2l=EdNbOV1NNn2+(Ep/32-muo(k))-2.0*Efl;
GdNbOV1NNn1l=EdNbOV1NNn1+(Ep/32-muo(k))-1.0*Efl;
GdNbOV1NN0l=EdNbOV1NN0+(Ep/32-muo(k))-0.0*Efl;
GdNbOV1NN1l=EdNbOV1NN1+(Ep/32-muo(k))+1.0*Efl;
GdNbOV1NN2l=EdNbOV1NN2+(Ep/32-muo(k))+2.0*Efl;
GdNbOV1NN3l=EdNbOV1NN3+(Ep/32-muo(k))+3.0*Efl;
%Nb substitution
GdNb_sub_n1l=EdNb_sub_n1+(Ep/32-2.0*muo(k))-1.0*Efl;
GdNb_sub_0l=EdNb_sub_0+(Ep/32-2.0*muo(k));
GdNb_sub_1l=EdNb_sub_1+(Ep/32-2.0*muo(k))+1.0*Efl;
if Gd1l<0.0 || Gd2l<0.0 || Gd3l<0.0 || Gd4l<0.0 ...
    || Gd5l<0.0 ...  || Gd6l<0.0 || GdV_4l<0.0 || GdV_3l<0.0...
    || GdV_2l<0.0 ...  || GdV_1l<0.0 || GdVl<0.0 || ...
    GdI4l<0.0 || GdI3l<0.0 ...  || GdI2l<0.0 || GdI1l<0.0...
    || GdIl<0.0 || GdNbIl<0.0 ...  || GdNbI1l<0.0 || GdNbI2l<0.0...
    || GdNbI3l<0.0...  || GdNbI4l<0.0 || GdNbI5l<0.0...
    || GdNbOV1NNn2l<0.0 || GdNbOV1NNn1l<0.0...
    || GdNbOV1NN0l<0.0 || GdNbOV1NN1l<0.0 || ...
    GdNbOV1NN2l<0.0 || GdNbOV1NN3l<0.0 ||...
    GdNb_sub_n1l<0.0 ...  || GdNb_sub_0l<0.0 ||...
    GdNb_sub_1l<0.0 Efl=Efl+0.0001;
```

```
    continue
end;
%!COMUTING THE NET CHARGED FOR
CONCENTRATIONS ON THE RIGHT AND LEFT
deno_OVr=1.0+exp(-beta*Gd1r)+exp(-beta*Gd2r)+exp(-beta*Gd3r);
deno_OIr=1.0+exp(-beta*Gd4r)+exp(-beta*Gd5r)+exp(-beta*Gd6r);
deno_ZVr=1.0+exp(-beta*GdV_4r)+exp(-beta*GdV_3r)...
+exp(-beta*GdV_2r)+exp(-beta*GdV_1r)+exp(-beta*GdVr);
deno_ZIr=1.0+exp(-beta*GdI4r)+exp(-beta*GdI3r)+exp(-beta*GdI2r)...
+exp(-beta*GdI1r)+exp(-beta*GdIr);
deno_NbIr=1.0+exp(-beta*GdNbIr)+exp(-beta*GdNbI1r)+...
exp(-beta*GdNbI2r)+exp(-beta*GdNbI3r)+exp(-beta*GdNbI4r)...
+exp(-beta*GdNbI5r);
deno_NbOV1NNr=1.0+exp(-beta*GdNbOV1NNn2r)...
+exp(-beta*GdNbOV1NNn1r)+exp(-beta*GdNbOV1NN0r)...
+exp(-beta*GdNbOV1NN1r)+exp(-beta*GdNbOV1NN2r)...
+exp(-beta*GdNbOV1NN3r);
deno_nb_subr=1.0+exp(-beta*GdNb_sub_n1r)...
+exp(-beta*GdNb_sub_0r)+exp(-beta*GdNb_sub_1r);
%!Oxygen Vacacnies
%COVr=(2.0*exp(-beta*Gd1r))/deno_OVr;
%2 is the number of possible places of vacacny per f.u.
COV1r=(2.0*exp(-beta*Gd2r))/deno_OVr;
COV2r=(2.0*exp(-beta*Gd3r))/deno_OVr;
%!Oxygen Interstitials
%COIr=(8.0*exp(-beta*Gd4r))/deno_OIr;
%8 is the number of possible ways of intersitial per f.u.
COI_1r=(8.0*exp(-beta*Gd5r))/deno_OIr;
COI_2r=(8.0*exp(-beta*Gd6r))/deno_OIr;
%!Zircnoium Vacancies
CZV_4r=exp(-beta*GdV_4r)/deno_ZVr;
%!Only one possible vacacny per formula unit
CZV_3r=exp(-beta*GdV_3r)/deno_ZVr;
CZV_2r=exp(-beta*GdV_2r)/deno_ZVr;
CZV_1r=exp(-beta*GdV_1r)/deno_ZVr;
%!CZVr=exp(-beta*GdVr)/deno_ZVr
%!Zircnoium Interstitials
%!CZIr=exp(-beta*GdIr)/deno_ZIr;
```

```
% Only one possible (octahedral site) per u.f
CZI1r=exp(-beta*GdI1r)/deno_ZIr; CZI2r=exp(-beta*GdI2r)/deno_ZIr;
CZI3r=exp(-beta*GdI3r)/deno_ZIr; CZI4r=exp(-beta*GdI4r)/deno_ZIr;
%!Electrons
%Cer=Ne*exp(-beta*(ECBM-Efr));
Cer=elec_conc_exp(Efr,beta,E_shift);
%!holes %Chr=Nh*exp(-beta*(Efr-EVBM));
Chr=hole_conc_exp(Efr,beta,E_shift);
%Nb interstitital
CNbIr=exp(-beta*GdNbIr)/deno_NbIr;
CNbI1r=exp(-beta*GdNbI1r)/deno_NbIr;
CNbI2r=exp(-beta*GdNbI2r)/deno_NbIr;
CNbI3r=exp(-beta*GdNbI3r)/deno_NbIr;
CNbI4r=exp(-beta*GdNbI4r)/deno_NbIr;
CNbI5r=exp(-beta*GdNbI5r)/deno_NbIr;
%O vacancy bound to Nb substitution
CNbOV1NNn2r=exp(-beta*GdNbOV1NNn2r)/deno_NbOV1NNr;
CNbOV1NNn1r=exp(-beta*GdNbOV1NNn1r)/deno_NbOV1NNr;
CNbOV1NNn0r=exp(-beta*GdNbOV1NN0r)/deno_NbOV1NNr;
CNbOV1NN1r=exp(-beta*GdNbOV1NN1r)/deno_NbOV1NNr;
CNbOV1NN2r=exp(-beta*GdNbOV1NN2r)/deno_NbOV1NNr;
CNbOV1NN3r=exp(-beta*GdNbOV1NN3r)/deno_NbOV1NNr;
% nb substitution
CNb_sub_n1r=exp(-beta*GdNb_sub_n1r)/deno_nb_subr;
CNb_sub_0r=exp(-beta*GdNb_sub_0r)/deno_nb_subr;
CNb_sub_1r=exp(-beta*GdNb_sub_1r)/deno_nb_subr;
deno_OVl=1.0+exp(-beta*Gd1l)+exp(-beta*Gd2l)+exp(-beta*Gd3l);
deno_OIl=1.0+exp(-beta*Gd4l)+exp(-beta*Gd5l)+exp(-beta*Gd6l);
deno_ZVl=1.0+exp(-beta*GdV_4l)+exp(-beta*GdV_3l)...
+exp(-beta*GdV_2l)+exp(-beta*GdV_1l)+exp(-beta*GdVl);
deno_ZIl=1.0+exp(-beta*GdI4l)+exp(-beta*GdI3l)...
+exp(-beta*GdI2l)+exp(-beta*GdI1l)+exp(-beta*GdIl);
deno_NbIl=1.0+exp(-beta*GdNbIl)+exp(-beta*GdNbI1l)...
+exp(-beta*GdNbI2l)+exp(-beta*GdNbI3l)...
+exp(-beta*GdNbI4l)+exp(-beta*GdNbI5l);
deno_NbOV1NNl=1.0+exp(-beta*GdNbOV1NNn2l)...
+exp(-beta*GdNbOV1NNn1l)+exp(-beta*GdNbOV1NN0l)...
+exp(-beta*GdNbOV1NN1l)+exp(-beta*GdNbOV1NN2l)+..
```

```
exp(-beta*GdNbOV1NN3l);deno_nb_subl=1.0...
+exp(-beta*GdNb_sub_n1l)...
+exp(-beta*GdNb_sub_0l)+exp(-beta*GdNb_sub_1l);
%!Oxygen Vacacnies
%COVl=(2.0*exp(-beta*Gd1l))/deno_OVl;
%2 is the number of possible places of vacacny per f.u.
COV1l=(2.0*exp(-beta*Gd2l))/deno_OVl;
COV2l=(2.0*exp(-beta*Gd3l))/deno_OVl;
%!Oxygen Interstitials
%!COIl=(8.0*exp(-beta*Gd4l))/deno_OIl;
%8 is the number of possible ways of intersitial per f.u.
COI_1l=(8.0*exp(-beta*Gd5l))/deno_OIl;
COI_2l=(8.0*exp(-beta*Gd6l))/deno_OIl;
%!Zirconium Vacancies
CZV_4l=exp(-beta*GdV_4l)/deno_ZVl;
%!Only one possible vacacny per formula unit
CZV_3l=exp(-beta*GdV_3l)/deno_ZVl;
CZV_2l=exp(-beta*GdV_2l)/deno_ZVl;
CZV_1l=exp(-beta*GdV_1l)/deno_ZVl;
%CZVl=exp(-beta*GdVl)/deno_ZVl;
%!Zirconium Interstitials
%!CZIl=exp(-beta*GdIl)/deno_ZIl;
% Only one possible (octahedral site) per u.f
CZI1l=exp(-beta*GdI1l)/deno_ZIl; CZI2l=exp(-beta*GdI2l)/deno_ZIl;
CZI3l=exp(-beta*GdI3l)/deno_ZIl; CZI4l=exp(-beta*GdI4l)/deno_ZIl;
%!Electrons %Cel=Ne*exp(-beta*(ECBM-Efl));
Cel=elec_conc_exp(Efl,beta,E_shift);
%!holes %Chl=Nh*exp(-beta*(Efl-EVBM));
Chl=hole_conc_exp(Efl,beta,E_shift);
%Nb interstitital
CNbIl=exp(-beta*GdNbIl)/deno_NbIl;
CNbI1l=exp(-beta*GdNbI1l)/deno_NbIl;
CNbI2l=exp(-beta*GdNbI2l)/deno_NbIl;
CNbI3l=exp(-beta*GdNbI3l)/deno_NbIl;
CNbI4l=exp(-beta*GdNbI4l)/deno_NbIl;
CNbI5l=exp(-beta*GdNbI5l)/deno_NbIl;
%O vacancy bound to Nb substitution
CNbOV1NNn2l=exp(-beta*GdNbOV1NNn2l)/deno_NbOV1NNl;
```

```
CNbOV1NNn1l=exp(-beta*GdNbOV1NNn1l)/deno_NbOV1NN1;
CNbOV1NNn0l=exp(-beta*GdNbOV1NN0l)/deno_NbOV1NN1;
CNbOV1NN1l=exp(-beta*GdNbOV1NN1l)/deno_NbOV1NN1;
CNbOV1NN2l=exp(-beta*GdNbOV1NN2l)/deno_NbOV1NN1;
CNbOV1NN3l=exp(-beta*GdNbOV1NN3l)/deno_NbOV1NN1;
% Nb substitution
CNb_sub_n1l=exp(-beta*GdNb_sub_n1l)/deno_nb_subl;
CNb_sub_0l=exp(-beta*GdNb_sub_0l)/deno_nb_subl;
CNb_sub_1l=exp(-beta*GdNb_sub_1l)/deno_nb_subl;
%Summations on the right and left
sum_right=-Cer+Chr+COV1r+2.0*COV2r-COI_1r-2.0*COI_2r...
-4.0*CZV_4r-3.0*CZV_3r-2.0*CZV_2r-CZV_1r+CZI1r+...
2.0*CZI2r+3.0*CZI3r+1.0*CNbI1r+2.0*CNbI2r+3.0*CNbI3r...
+4.0*CNbI4r+5.0*CNbI5r-2.0*CNbOV1NNn2r-...
1.0*CNbOV1NNn1r+1.0*CNbOV1NN1r+2.0*CNbOV1NN2r...
+3.0*CNbOV1NN3r-1.0*CNb_sub_n1r+1.0*CNb_sub_1r;
sum_right=sum_right+4.0*CZI4r;
sum_left=-Cel+Chl+COV1l+2.0*COV2l-COI_1l-2.0*COI_2l...
-4.0*CZV_4l-3.0*CZV_3l-2.0*CZV_2l-CZV_1l+CZI1l...
+2.0*CZI2l+3.0*CZI3l+1.0*CNbI1l+2.0*CNbI2l+3.0*CNbI3l...
+4.0*CNbI4l+5.0*CNbI5l-2.0*CNbOV1NNn2l-1.0*CNbOV1NNn1l...
+1.0*CNbOV1NN1l+2.0*CNbOV1NN2l+3.0*CNbOV1NN3l...
-1.0*CNb_sub_n1l+1.0*CNb_sub_1l;
sum_left=sum_left+4.0*CZI4l;
%CHECK IF YOU ARE BRACKETING THE ROOT OR NOT
if sum_right*sum_left>0.0 || Efl>Efr
    Ef(k)=20; Ce(k)=20; Ch(k)=20; COV(k)=20; COV1(k)=20;
    COV2(k)=20; COI(k)=20; COI_1(k)=20; COI_2(k)=20;
    CZV_4(k)=20; CZV_3(k)=20; CZV_2(k)=20; CZV_1(k)=20;
    CZV(k)=20; CZI(k)=20; CZI1(k)=20; CZI2(k)=20; CZI3(k)=20;
    CZI4(k)=20; CNbI(k)=20; CNbI1(k)=20; CNbI2(k)=20;
    CNbI3(k)=20;
    CNbI4(k)=20; CNbI5(k)=20; CNbOV1NNn2(k)=20;
    CNbOV1NNn1(k)=20;
    CNbOV1NN0(k)=20; CNbOV1NN1(k)=20; CNbOV1NN2(k)=20;
    CNbOV1NN3(k)=20; CNb_sub_n1(k)=20; CNb_sub_0(k)=20;
    CNb_sub_1(k)=20;
    old_root=0.0; no_solution=1;
```

```
    break
end;
new_root=(Efr+Efl)/2.0; Ef(k)=new_root;
%!Computing the concentraions at the new root
%!Oxygen VACACNY
Gd1(k)=Ed1+muo(k);
Gd2(k)=Ed2+muo(k)+Ef(k);
Gd3(k)=Ed3+muo(k)+2.0*Ef(k);
%!Oxygen Interstitial Interstitial
Gd4(k)=Ed4-muo(k);
Gd5(k)=Ed5-muo(k)-Ef(k);
Gd6(k)=Ed6-muo(k)-2.0*Ef(k);
%!Zircnoium Vacacny
GdV_4(k)=EdV_4-2.0*muo(k)-4.0*Ef(k);
GdV_3(k)=EdV_3-2.0*muo(k)-3.0*Ef(k);
GdV_2(k)=EdV_2-2.0*muo(k)-2.0*Ef(k);
GdV_1(k)=EdV_1-2.0*muo(k)-Ef(k);
GdV(k)=EdV-2.0*muo(k);
%!interstitial Zirconium
GdI(k)=EdI+2.0*muo(k);
GdI1(k)=EdI1+2.0*muo(k)+Ef(k);
GdI2(k)=EdI2+2.0*muo(k)+2.0*Ef(k);
GdI3(k)=EdI3+2.0*muo(k)+3.0*Ef(k);
GdI4(k)=EdI4+2.0*muo(k)+4.0*Ef(k);
% nb interstitial
GdNbI(k)=EdNbI; GdNbI1(k)=EdNbI1+1.0*Ef(k);
GdNbI2(k)=EdNbI2+2.0*Ef(k); GdNbI3(k)=EdNbI3+3.0*Ef(k);
GdNbI4(k)=EdNbI4+4.0*Ef(k); GdNbI5(k)=EdNbI5+5.0*Ef(k);
% oxygen vacancy bound to Nb substitution
GdNbOV1NNn2(k)=EdNbOV1NNn2+(Ep/32-muo(k))-2.0*Ef(k);
GdNbOV1NNn1(k)=EdNbOV1NNn1+(Ep/32-muo(k))-1.0*Ef(k);
GdNbOV1NN0(k)=EdNbOV1NN0+(Ep/32-muo(k))-0.0*Ef(k);
GdNbOV1NN1(k)=EdNbOV1NN1+(Ep/32-muo(k))+1.0*Ef(k);
GdNbOV1NN2(k)=EdNbOV1NN2+(Ep/32-muo(k))+2.0*Ef(k);
GdNbOV1NN3(k)=EdNbOV1NN3+(Ep/32-muo(k))+3.0*Ef(k);
% Nb substitution
GdNb_sub_n1(k)=EdNb_sub_n1+(Ep/32-2.0*muo(k))-1.0*Ef(k);
GdNb_sub_0(k)=EdNb_sub_0+(Ep/32-2.0*muo(k));
```

```
GdNb_sub_1(k)=EdNb_sub_1+(Ep/32-2.0*muo(k))+1.0*Ef(k);
deno_OV=1.0+exp(-beta*Gd1(k))+exp(-beta*Gd2(k))...

+exp(-beta*Gd3(k));

deno_OI=1.0+exp(-beta*Gd4(k))+exp(-beta*Gd5(k))...

+exp(-beta*Gd6(k));

deno_ZV=1.0+exp(-beta*GdV_4(k))+exp(-beta*GdV_3(k))+...
exp(-beta*GdV_2(k))+exp(-beta*GdV_1(k))+exp(-beta*GdV(k));
deno_ZI=1.0+exp(-beta*GdI4(k))+exp(-beta*GdI3(k))+...
exp(-beta*GdI2(k))+exp(-beta*GdI1(k))+exp(-beta*GdI(k));
deno_NbI=1.0+exp(-beta*GdNbI(k))+exp(-beta*GdNbI1(k))+...
exp(-beta*GdNbI2(k))+exp(-beta*GdNbI3(k))+...
exp(-beta*GdNbI4(k))+exp(-beta*GdNbI5(k));
deno_NbOV1NN=1.0+exp(-beta*GdNbOV1NNn2(k))...
+exp(-beta*GdNbOV1NNn1(k))+exp(-beta*GdNbOV1NN0(k))...
+exp(-beta*GdNbOV1NN1(k))+exp(-beta*GdNbOV1NN2(k))...
+exp(-beta*GdNbOV1NN3(k));
deno_nb_sub=1.0+exp(-beta*GdNb_sub_n1(k))+...
exp(-beta*GdNb_sub_0(k))+exp(-beta*GdNb_sub_1(k));
%!Oxygen Vacacnies
COV(k)=(2.0*exp(-beta*Gd1(k)))/deno_OV;
%2 is the number of possible places of vacacny per f.u.
COV1(k)=(2.0*exp(-beta*Gd2(k)))/deno_OV;
COV2(k)=(2.0*exp(-beta*Gd3(k)))/deno_OV;
%!Oxygen Interstitials
COI(k)=(8.0*exp(-beta*Gd4(k)))/deno_OI;
% 8 is the number of possible ways of intersitial per f.u.
COI_1(k)=(8.0*exp(-beta*Gd5(k)))/deno_OI;
COI_2(k)=(8.0*exp(-beta*Gd6(k)))/deno_OI;
%!Zirconium Vacancies
CZV_4(k)=exp(-beta*GdV_4(k))/deno_ZV;
%Only one possible vacacny per f.u
CZV_3(k)=exp(-beta*GdV_3(k))/deno_ZV;
CZV_2(k)=exp(-beta*GdV_2(k))/deno_ZV;
CZV_1(k)=exp(-beta*GdV_1(k))/deno_ZV;
CZV(k)=exp(-beta*GdV(k))/deno_ZV;
```

```
%Zirconium Interstitials
CZI(k)=exp(-beta*GdI(k))/deno_ZI;%
% Only one possible (octahedral site) per u.f
CZI1(k)=exp(-beta*GdI1(k))/deno_ZI;
CZI2(k)=exp(-beta*GdI2(k))/deno_ZI;
CZI3(k)=exp(-beta*GdI3(k))/deno_ZI;
CZI4(k)=exp(-beta*GdI4(k))/deno_ZI;
%!Electrons
%Ce(k)=Ne*exp(-beta*(ECBM-Ef(k)));
Ce(k)=elec_conc_exp(Ef(k),beta,E_shift);
%!holes
%Ch(k)=Nh*exp(-beta*(Ef(k)-EVBM));
Ch(k)=hole_conc_exp(Ef(k),beta,E_shift);
%Nb interstitial
CNbI(k)=exp(-beta*GdNbI(k))/deno_NbI;
CNbI1(k)=exp(-beta*GdNbI1(k))/deno_NbI;
CNbI2(k)=exp(-beta*GdNbI2(k))/deno_NbI;
CNbI3(k)=exp(-beta*GdNbI3(k))/deno_NbI;
CNbI4(k)=exp(-beta*GdNbI4(k))/deno_NbI;
CNbI5(k)=exp(-beta*GdNbI5(k))/deno_NbI;
% Oxygen vacancy bound to Nb substitution
CNbOV1NNn2(k)=exp(-beta*GdNbOV1NNn2(k))/deno_NbOV1NN;
CNbOV1NNn1(k)=exp(-beta*GdNbOV1NNn1(k))/deno_NbOV1NN;
CNbOV1NN0(k)=exp(-beta*GdNbOV1NN0(k))/deno_NbOV1NN;
CNbOV1NN1(k)=exp(-beta*GdNbOV1NN1(k))/deno_NbOV1NN;
CNbOV1NN2(k)=exp(-beta*GdNbOV1NN2(k))/deno_NbOV1NN;
CNbOV1NN3(k)=exp(-beta*GdNbOV1NN3(k))/deno_NbOV1NN;
% Nb substitution
CNb_sub_n1(k)=exp(-beta*GdNb_sub_n1(k))/deno_nb_sub;
CNb_sub_0(k)=exp(-beta*GdNb_sub_0(k))/deno_nb_sub;
CNb_sub_1(k)=exp(-beta*GdNb_sub_1(k))/deno_nb_sub;
%Convergence TEST
relative_error=(new_root-old_root)/new_root;
relative_error=abs(relative_error);
if relative_error<prec
    old_root=0.0;
    new_root v=v+1; %!The counter of physical pressures
    w=[w k]; %!locate reasonable pressures
```

```
            Fermi_energies=[Fermi_energies new_root];
            break
        end;
        sum_root=-Ce(k)+Ch(k)+COV1(k)+2.0*COV2(k)-COI_1(k)-...
        2.0*COI_2(k)-4.0*CZV_4(k)-3.0*CZV_3(k)-2.0*CZV_2(k)-...
        CZV_1(k)+1.0*CNbI1(k)+2.0*CNbI2(k)+3.0*CNbI3(k)+...
        4.0*CNbI4(k)+5.0*CNbI5(k)-2.0*CNbOV1NNn2(k)-...
        1.0*CNbOV1NNn1(k)+1.0*CNbOV1NN1(k)+2.0*CNbOV1NN2(k)+...
        3.0*CNbOV1NN3(k)-1.0*CNb_sub_n1(k)+1.0*CNb_sub_1(k);
        sum_root=sum_root+CZI1(k)+2.0*CZI2(k)+3.0*CZI3(k)+4.0*CZI4(k);
        if sum_left*sum_root<0.0
            Efr=new_root; old_root=new_root;
        elseif sum_left*sum_root>=0.0
            Efl=new_root; old_root=new_root;
        end;
    end;
    if no_solution==1
        continue
    end;
end;
%!COMPUTING THE NON_STOICHIOMETRY x
x=zeros(1,n); GdV_test=zeros(1,n);
for k=1:v
    a=COI(w(k))+COI_1(w(k))+COI_2(w(k))-COV(w(k))-...
    COV1(w(k))-COV2(w(k));
    delta=CZI(w(k))+CZI1(w(k))+CZI2(w(k))+...
    CZI3(w(k))+CZI4(w(k))-CZV(w(k))-CZV_1(w(k))...
    -CZV_2(w(k))-CZV_3(w(k))-CZV_4(w(k));
    x(w(k))=((2.0+a)/(1.0+delta))-2.0;
end;
%plot(x) z=zeros(1,n);
for k=1:v
    z(w(k))=1;
end;
%!TAKING THE LOG pf the CONCENTRAION
concentration_matrix=[];
CNb=log10(CNbI+CNbI1+CNbI2+CNbI3+CNbI4...
+CNbI5+CNbOV1NNn2+CNbOV1NNn1+CNbOV1NN0+
```

```
...  CNbOV1NN1+CNbOV1NN2+CNb_sub_n1+CNb_sub_0+CNb_sub_1);
concentration_matrix=...  [concentration_matrix;CNb];
CNb5=log10(CNbI5+CNb_sub_1);
CNb4=log10(CNbI4+CNbOV1NN2+CNbOV1NN0+CNb_sub_0);
CNb3=log10(CNbI3+CNbOV1NN1+CNbOV1NNn1+CNb_sub_n1);
Ce=log10(Ce);concentration_matrix=[concentration_matrix;Ce];
Ch=log10(Ch);concentration_matrix=[concentration_matrix;Ch];
COI=log10(COI);concentration_matrix=[concentration_matrix;COI];
COI_1=log10(COI_1);concentration_matrix=[concentration_matrix;COI_1];
COI_2=log10(COI_2);concentration_matrix=[concentration_matrix;COI_2];
COV=log10(COV);concentration_matrix=[concentration_matrix;COV];
COV1=log10(COV1);concentration_matrix=[concentration_matrix;COV1];
COV2=log10(COV2);concentration_matrix=[concentration_matrix;COV2];
CZI=log10(CZI);concentration_matrix=[concentration_matrix;CZI];
CZI1=log10(CZI1);concentration_matrix=[concentration_matrix;CZI1];
CZI2=log10(CZI2);concentration_matrix=[concentration_matrix;CZI2];
CZI3=log10(CZI3);concentration_matrix=[concentration_matrix;CZI3];
CZI4=log10(CZI4);concentration_matrix=[concentration_matrix;CZI4];
CZV=log10(CZV);concentration_matrix=[concentration_matrix;CZV];
CZV_1=log10(CZV_1);concentration_matrix=[concentration_matrix;CZV_1];
CZV_2=log10(CZV_2);concentration_matrix=[concentration_matrix;CZV_2];
CZV_3=log10(CZV_3);concentration_matrix=[concentration_matrix;CZV_3];
CZV_4=log10(CZV_4);concentration_matrix=[concentration_matrix;CZV_4];
CNbI=log10(CNbI);concentration_matrix=[concentration_matrix;CNbI];
CNbI1=log10(CNbI1);concentration_matrix=[concentration_matrix;CNbI1];
CNbI2=log10(CNbI2);concentration_matrix=[concentration_matrix;CNbI2];
CNbI3=log10(CNbI3);concentration_matrix=[concentration_matrix;CNbI3];
CNbI4=log10(CNbI4);concentration_matrix=[concentration_matrix;CNbI4];
CNbI5=log10(CNbI5);concentration_matrix=[concentration_matrix;CNbI5];
CNbOV1NNn2=log10(CNbOV1NNn2);
concentration_matrix=[concentration_matrix;CNbOV1NNn2];
CNbOV1NNn1=log10(CNbOV1NNn1);
concentration_matrix=[concentration_matrix;CNbOV1NNn1];
CNbOV1NN0=log10(CNbOV1NN0);
concentration_matrix=[concentration_matrix;CNbOV1NN0];
CNbOV1NN1=log10(CNbOV1NN1);
concentration_matrix=[concentration_matrix;CNbOV1NN1];
CNbOV1NN2=log10(CNbOV1NN2);
```

```
concentration_matrix=[concentration_matrix;CNbOV1NN2];
CNb_sub_n1=log10(CNb_sub_n1);
concentration_matrix=[concentration_matrix;CNb_sub_n1];
CNb_sub_0=log10(CNb_sub_0);
concentration_matrix=[concentration_matrix;CNb_sub_0];
CNb_sub_1=log10(CNb_sub_1);
concentration_matrix=[concentration_matrix;CNb_sub_1];
logPO2_purezirconia=logPO2; Ce_purezirconia=Ce;
Ch_purezirconia=Ch; COV_purezirconia=COV;
COV2_purezirconia=COV2; CZI4_purezirconia=CZI4;
CZV_4_purezirconia=CZV_4;
Ef=Ef-EVBM;
size_values=size(concentration_matrix); answer=[];
for i=1:size_values(1)
    if concentration_matrix(i,w(1))>-10
        answer=[answer i];
    end;
end;
x_test=[];
Gd1_test=[]; Gd2_test=[]; Gd3_test=[]; Gd4_test=[]; Gd5_test=[];
Gd6_test=[]; GdV_4_test=[]; GdV_3_test=[]; GdV_2_test=[];
GdV_1_test=[]; GdV_test=[]; GdI_test=[]; GdI1_test=[]; GdI2_test=[];
GdI3_test=[]; GdI4_test=[]; GdNbI_test=[];GdNbI1_test=[];
GdNbI2_test=[]; GdNbI3_test=[]; GdNbI4_test=[]; GdNbI5_test=[];
GdNbOV1NNn2_test=[]; GdNbOV1NNn1_test=[]; GdNbOV1NN0_test=[];
GdNbOV1NN1_test=[]; GdNbOV1NN2_test=[]; GdNbOV1NN3_test=[];
GdNb_sub_n1_test=[]; GdNb_sub_0_test=[]; GdNb_sub_1_test=[];
logPO2_test=[]; Fermi_energies_pure=[];
for k=1:v
    if x(w(k))<0.064516129032258 && x(w(k))>-0.064516129032258
        x_test=[x_test x(w(k))]; Gd1_test=[Gd1_test Gd1(w(k))];
        Gd2_test=[Gd2_test Gd2(w(k))]; Gd3_test=[Gd3_test Gd3(w(k))];
        Gd4_test=[Gd4_test Gd4(w(k))]; Gd5_test=[Gd5_test Gd5(w(k))];
        Gd6_test=[Gd6_test Gd6(w(k))];
        GdV_4_test=[GdV_4_test GdV_4(w(k))];
        GdV_3_test=[GdV_3_test GdV_3(w(k))];
        GdV_2_test=[GdV_2_test GdV_2(w(k))];
        GdV_1_test=[GdV_1_test GdV_1(w(k))];
```

```
        GdV_test=[GdV_test GdV(w(k))];
        GdI_test=[GdI_test GdI(w(k))];
        GdI1_test=[GdI1_test GdI1(w(k))];
        GdI2_test=[GdI2_test GdI2(w(k))];
        GdI3_test=[GdI3_test GdI3(w(k))];
        GdI4_test=[GdI4_test GdI4(w(k))];
        GdNbI_test=[GdNbI_test GdI(w(k))];
        GdNbI1_test=[GdNbI1_test GdNbI1(w(k))];
        GdNbI2_test=[GdNbI2_test GdNbI2(w(k))];
        GdNbI3_test=[GdNbI3_test GdNbI3(w(k))];
        GdNbI4_test=[GdNbI4_test GdNbI4(w(k))];
        GdNbOV1NNn2_test=[GdNbOV1NNn2_test GdNbOV1NNn2(w(k))];
        GdNbOV1NNn1_test=[GdNbOV1NNn1_test GdNbOV1NNn1(w(k))];
        GdNbOV1NN0_test=[GdNbOV1NN0_test GdNbOV1NN0(w(k))];
        GdNbOV1NN1_test=[GdNbOV1NN1_test GdNbOV1NN1(w(k))];
        GdNbOV1NN2_test=[GdNbOV1NN2_test GdNbOV1NN2(w(k))];
        GdNbOV1NN3_test=[GdNbOV1NN3_test GdNbOV1NN3(w(k))];
        GdNb_sub_n1_test=[GdNb_sub_n1_test GdNb_sub_n1(w(k))];
        GdNb_sub_0_test=[GdNb_sub_0_test GdNb_sub_0(w(k))];
        GdNb_sub_1_test=[GdNb_sub_1_test GdNb_sub_1(w(k))];
        logPO2_test=[logPO2_test logPO2(w(k))];
        Fermi_energies_pure=[Fermi_energies_pure Fermi_energies(k)];
    end;
end;
logPO2_pure=logPO2_test; x_test_pure=x_test;
p_test=[]; Ce_test=[]; Ch_test=[]; COV_test=[]; COV1_test=[];
COV2_test=[]; COI_test=[]; COI_1_test=[]; COI_2_test=[];
CZV_test=[]; CZV_1_test=[]; CZV_2_test=[]; CZV_3_test=[];
CZV_4_test=[]; CZI_test=[]; CZI1_test=[]; CZI2_test=[];
CZI3_test=[]; CZI4_test=[]; CNbI_test=[]; CNbI1_test=[];
CNbI2_test=[];%21 CNbI3_test=[];%22 CNbI4_test=[];
CNbI5_test=[];%24 CNbOV1NNn2_test=[];
CNbOV1NNn1_test=[]; CNbOV1NN0_test=[]; CNbOV1NN1_test=[];
CNbOV1NN2_test=[]; CNb_sub_n1_test=[];CNb_sub_0_test=[];
CNb_sub_1_test=[];%32 CNb_test=[]; CNb5_test=[]; CNb4_test=[];
CNb3_test=[];
for k=1:v
    if x(w(k))< 0.064516129032258 && x(w(k))>-0.064516129032258
```

```
        p_test=[p_test logPO2(w(k))]; Ce_test=[Ce_test Ce(w(k))];
        Ch_test=[Ch_test Ch(w(k))]; COV_test=[COV_test COV(w(k))];
        COV1_test=[COV1_test COV1(w(k))];
        COV2_test=[COV2_test COV2(w(k))];
        COI_test=[COI_test COI(w(k))];
        COI_1_test=[COI_1_test COI_1(w(k))];
        COI_2_test=[COI_2_test COI_2(w(k))];
        CZV_test=[CZV_test CZV(w(k))];
        CZV_1_test=[CZV_1_test CZV_1(w(k))];
        CZV_2_test=[CZV_2_test CZV_2(w(k))];
        CZV_3_test=[CZV_3_test CZV_3(w(k))];
        CZV_4_test=[CZV_4_test CZV_4(w(k))];
        CZI_test=[CZI_test CZI(w(k))];
        CZI1_test=[CZI1_test CZI1(w(k))];
        CZI2_test=[CZI2_test CZI2(w(k))];
        CZI3_test=[CZI3_test CZI3(w(k))];
        CZI4_test=[CZI4_test CZI4(w(k))];
        CNbI_test=[CNbI_test CNbI(w(k))];
        CNbI1_test=[CNbI1_test CNbI1(w(k))];
        CNbI2_test=[CNbI2_test CNbI2(w(k))];
        CNbI3_test=[CNbI3_test CNbI3(w(k))];
        CNbI4_test=[CNbI4_test CNbI4(w(k))];
        CNbI5_test=[CNbI5_test CNbI5(w(k))];
        CNbOV1NNn2_test=[CNbOV1NNn2_test CNbOV1NNn2(w(k))];
        CNbOV1NNn1_test=[CNbOV1NNn1_test CNbOV1NNn1(w(k))];
        CNbOV1NN0_test=[CNbOV1NN0_test CNbOV1NN0(w(k))];
        CNbOV1NN1_test=[CNbOV1NN1_test CNbOV1NN1(w(k))];
        CNbOV1NN2_test=[CNbOV1NN2_test CNbOV1NN2(w(k))];
        CNb_sub_n1_test=[CNb_sub_n1_test CNb_sub_n1(w(k))];
        CNb_sub_0_test=[CNb_sub_0_test CNb_sub_0(w(k))];
        CNb_sub_1_test=[CNb_sub_1_test CNb_sub_1(w(k))];
        CNb_test=[CNb_test CNb(w(k))];
        CNb5_test=[CNb5_test CNb5(w(k))];
        CNb4_test=[CNb4_test CNb4(w(k))];
        CNb3_test=[CNb3_test CNb3(w(k))];
    end;
end;
Figure1 = figure;
```

```
Axes1 = axes('Parent',figure1);
axis square set(axes1,'FontSize',16)
xlabel('log_{10}P_{O_2}(atm)')
ylabel('log_{10}[D](per ZrO_2)')
xlim(axes1,[-15 0]);
ylim(axes1,[-8 -2]);
box(axes1,'on');
hold(axes1,'all');
y=[Ce_test;COV_test;COV2_test;CZV_4_test;Ch_test;CNb_sub_1_test];
plot1 = plot(p_test,y,'Parent',axes1,'LineWidth', 2.5);
plot1 = plot(log10(abs(x_test(1:17))),y(:,1:17),...

'Parent',axes1,'LineWidth', 2.5);

set(plot1(1),'DisplayName','Ce pure');
set(plot1(2),'DisplayName','COV pure');
set(plot1(3),'DisplayName','COV2 pure');
set(plot1(4),'DisplayName','CZV_4 pure');
set(plot1(5),'DisplayName','Ch pure');
set(plot1(6),'DisplayName','CNb_sub_1');
legend1 = legend(axes1,'show'); set(legend1,...  'Position',
[0.659996890547264 0.61701065464457 0.182089552238806 0.328136599851522]);
```